

Supplementary Material for

EF-hand Protein Ca^{2+} Buffers Regulate Ca^{2+} Influx and Exocytosis in Sensory Hair Cells

by

Tina Pangršič, Mantas Gabrielaitis, Susann Michanski, Beat Schwaller, Fred Wolf, Nicola Strenzke,
Tobias Moser

Contents

| | | |
|----------|--|-----------|
| 1 | Supplementary Figure 1 | 2 |
| 2 | Supplementary Figure 2 | 3 |
| 3 | Supplementary Figure 3 | 4 |
| 4 | Supplementary Figure 4 | 5 |
| 5 | Supplementary Figure 5 | 6 |
| 6 | Supplementary Figure 6 | 7 |
| 7 | Modeling of Ca^{2+} Dynamics (Including Supplementary Figures 7 – 11) | 8 |
| 7.1 | Reaction-Diffusion equations for $[\text{Ca}^{2+}]$ dynamics | 8 |
| 7.2 | Temporal evolution of $[\text{Ca}^{2+}]$ | 10 |
| 7.3 | Extent of Ca^{2+} buffer depletion due to Ca^{2+} influx | 12 |
| 7.4 | Influence of the partial buffer depletion on the $[\text{Ca}^{2+}]$ vs. i_{Ca} relation | 12 |
| 7.5 | Effect of accumulated bulk Ca^{2+} during prolonged stimulation on the model predictions of concentrations of the endogenous Ca^{2+} buffers | 14 |
| 7.6 | Influence of the type of boundary conditions on the estimates of the endogenous buffer concentrations and the coupling distance R_c | 15 |
| 8 | Defining and Evaluating the Effective Coupling Distance R_c (Including Supplementary Figure 12) | 17 |
| 8.1 | Active zones with 1 vesicular release site and N Ca^{2+} channels, no Ca^{2+} buffers | 17 |
| 8.2 | Active zones with 1 vesicular release site and N Ca^{2+} channels, one set of Ca^{2+} buffers | 19 |
| 8.3 | Active zones with 1 vesicular release site and N Ca^{2+} channels, two sets of Ca^{2+} buffers | 21 |
| 8.4 | Active zones with M vesicular release sites and N Ca^{2+} channels | 23 |
| 8.5 | Influence of the Ca^{2+} channel opening-closing dynamics on R_c estimate | 26 |
| | References | 28 |

1 Supplementary Figure 1

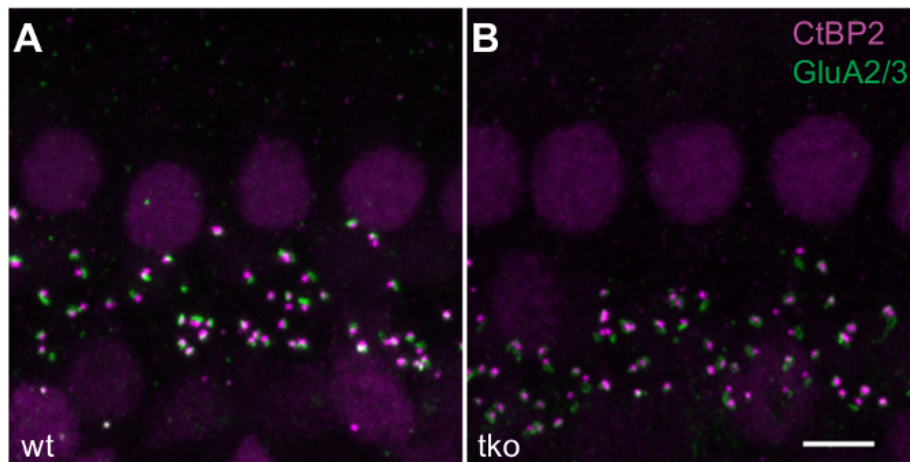


Figure S1: Comparable number of ribbon synapses in the IHCs of the triple buffer knockout and wild-type mice. (A – B) Confocal images of whole-mounts of organs of Corti double stained for the presynaptic marker CtBP2/Ribeye (magenta) and postsynaptic marker GluA 2/3 (green). The number of synapses in tko IHCs (B) was comparable to that of wt IHCs (A). Intact synapses are defined by the juxtaposition of pairs of pre- and postsynaptic fluorescent spots. Scale bar: 5 μm .

2 Supplementary Figure 2

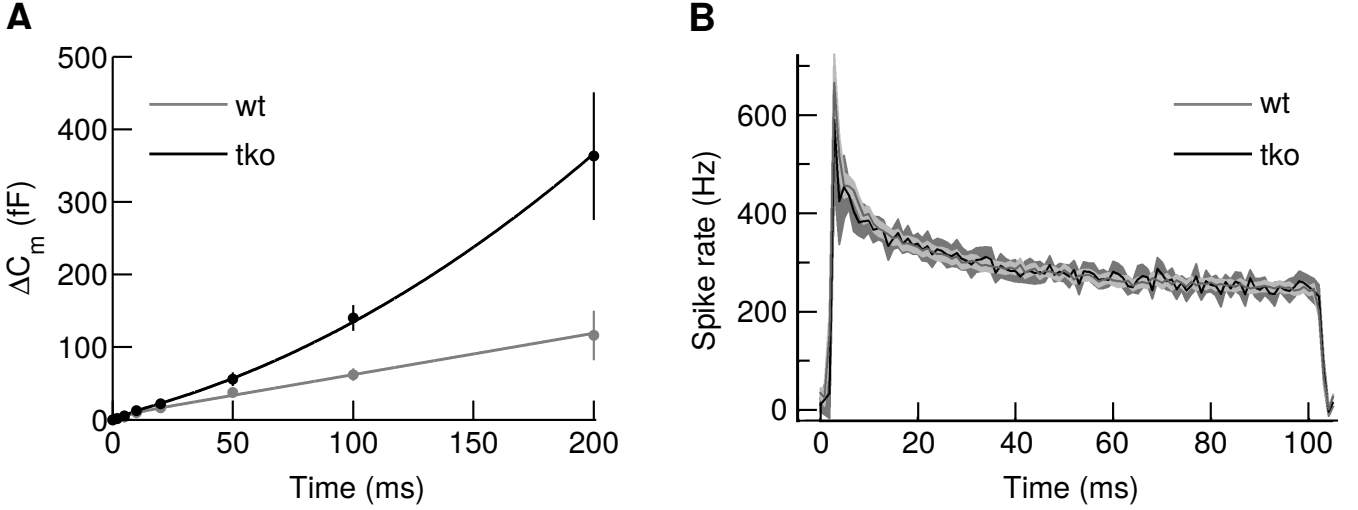


Figure S2: Cumulative exocytosis and SGN spike rates in response to prolonged stimuli in wt and tko mice. (A) Phenomenological fits to the experimental $\Delta C_m(t)$ data. The wt data were fitted by $\Delta C_m(t) = A' \cdot t + B' \cdot (1 - e^{-t/\tau})^n$ with (A', B', τ, n) treated as fitting parameters. The tko data were fitted by $\Delta C_m(t) = A' \cdot t + B' \cdot (1 - e^{-t/\tau})^n + t \cdot (a' \cdot t + b')$ with parameters (A', B', τ, n) set to the same values as for the wt data. Parameters a' and b' were found by fitting the difference between the experimental estimates of $\Delta C_m(t)$ from tko and wt IHCs by $t \cdot (a' \cdot t + b')$. Note that parameters (A, B, a, b) considered in Methods section “Conversion of neurotransmitter release events to spikes” correspond to the parameters (A', B', a', b') multiplied by $sc/(C_{sv} \cdot N_{syn})$. (B) Mean peristimulus time histogram (\pm s.e.m.), plotting the instantaneous spiking rate in 1-ms time bins over the time course of stimulation with 100 ms long tone bursts at the characteristic frequency of each SGN, 30 dB above threshold. The rates and the time course of adaptation were similar in tko (grey, $n = 35$) and wt SGNs (black, $n = 8$).

3 Supplementary Figure 3

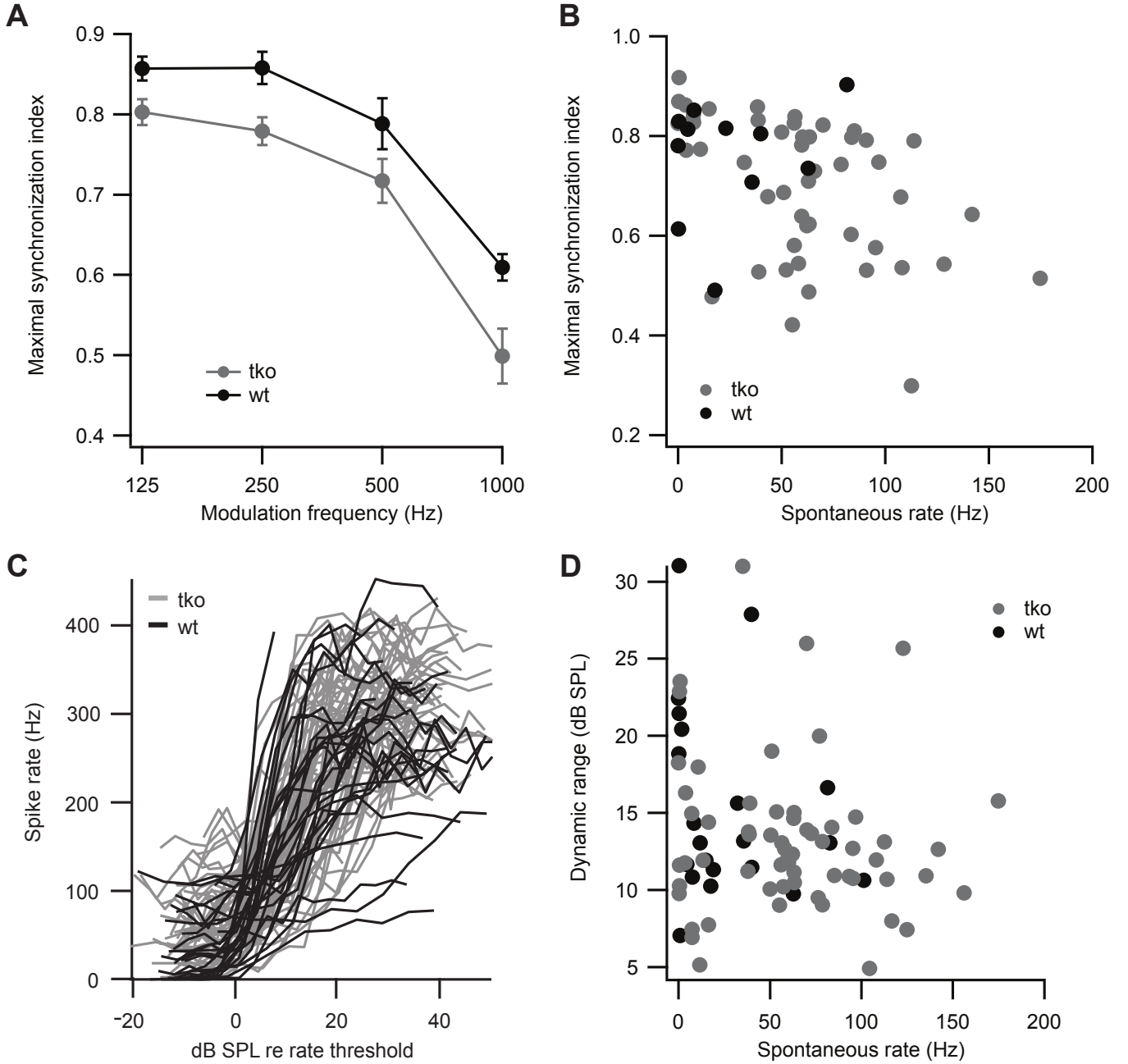


Figure S3: Precision of ongoing sound encoding is not affected by the absence of the three Ca^{2+} buffers. (A) Synchronization of SGN spiking to amplitude modulated transposed tones (formed by modulating a continuous sine wave at CF by a half-wave rectified sinusoid) was assessed at several stimulus intensities and modulation frequencies to determine the maximal synchronization index. (B) Maximal synchronization at 500 Hz was comparable between tko (grey, $n = 49$) and wt SGNs (black, $n = 11$) in spite of the tendency towards higher spontaneous rates in tko. (C) The steepness of spike rate increase with tone burst intensities was unchanged between tko (grey, $n = 64$) and wt (black, $n = 22$) SGNs. (D) The dynamic range of sound encoding (range of intensities over which the spike rate increases), which co-varies with spontaneous spiking rate, was similar among genotypes.

4 Supplementary Figure 4

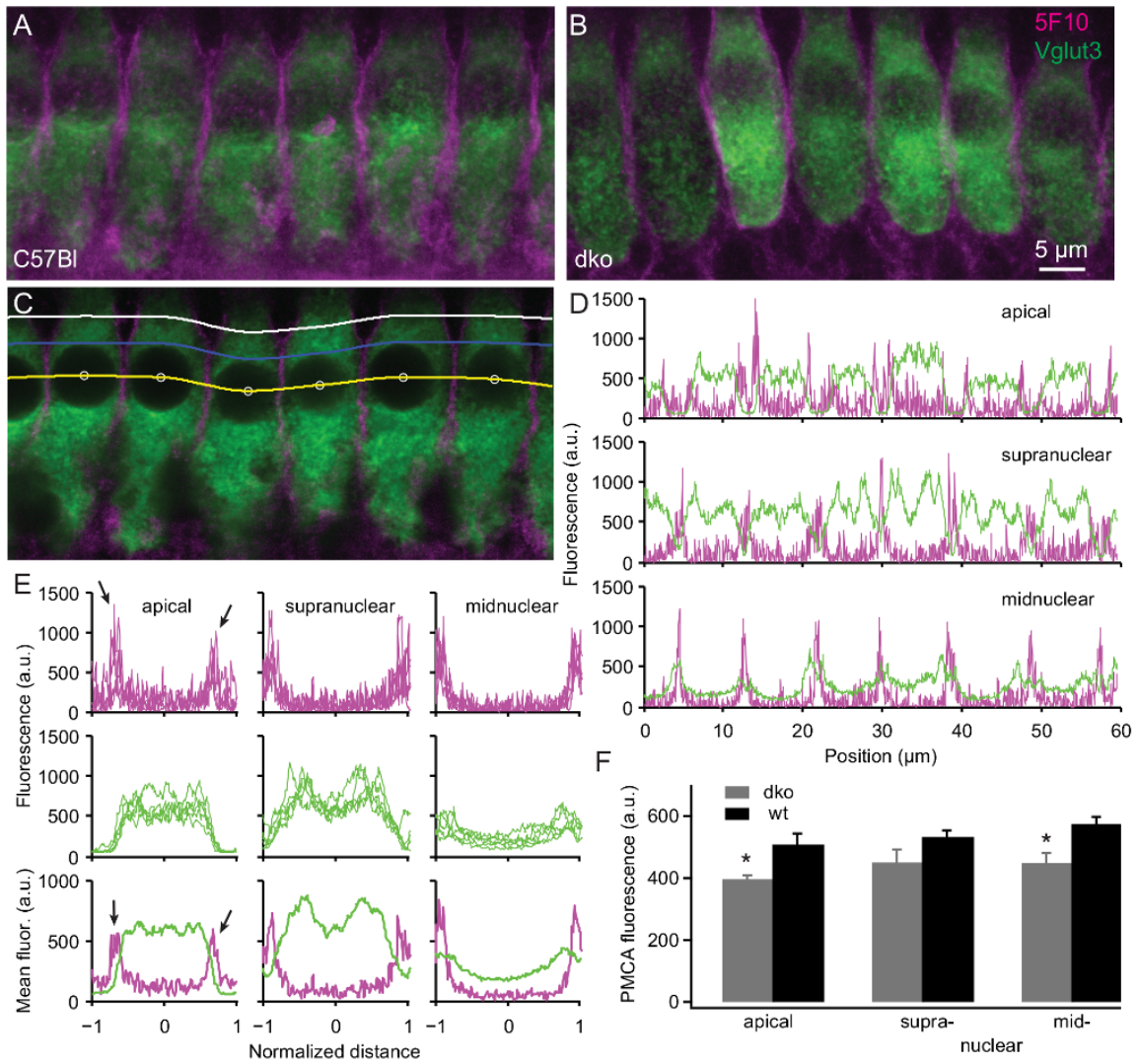


Figure S4: No compensatory upregulation of Ca^{2+} ATPases (PMCAs) in the plasma membrane of the double buffer knockout IHCs. (A-B) Maximal projections of confocal image stacks of a wt (A) and a dko (B) organ of Corti, stained for panPMCA (5F10, magenta) and an IHC marker Vglut3 (green). (C-E) An example demonstrating how the analysis of the PMCA fluorescence intensity was performed. (C) For each z-stack the immunofluorescence intensity was analyzed in the image plane with the best discernible nuclei (white circles denoting their centers). (D) Line profiles of Vglut3 (green) and PMCA (magenta) fluorescence intensity in the apical, supranuclear and midnuclear IHC region (white, blue and yellow line in panel C, respectively). Please note that we restricted our analysis to these cellular regions because the PMCA immunofluorescence was less well discernible in the basal parts of IHCs of either genotype (due to strong fluorescence in the surrounding tissue, e.g., the nerve fibers). (E) Fluorescence line profiles (from D) of separate cells aligned and superimposed (upper and middle panels). Lower panels show grand averages. Note a visible increase in the PMCA immunofluorescence at the cell borders (arrows). The average fluorescence intensity of these peaks was taken as the IHC PMCA fluorescence. (F) Histogram of average PMCA immunofluorescence in the three cellular regions. Note a significant decrease in the PMCA fluorescence in the plasma membranes of dko IHCs as compared to wt controls (Wilcoxon rank sum test, asterisks, $p < 0.05$).

5 Supplementary Figure 5

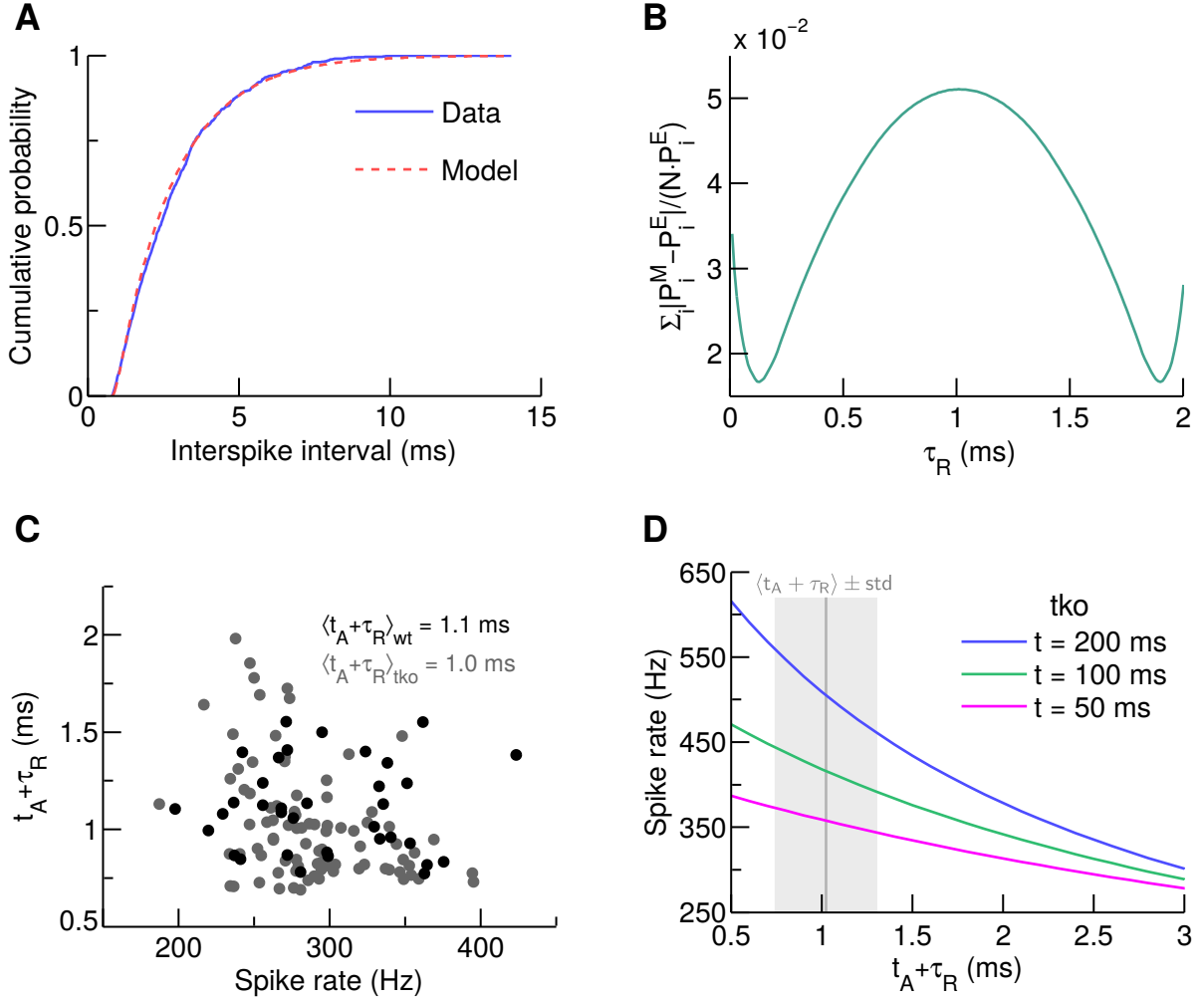


Figure S5: Estimation of the refractory periods and their impact on the discrepancy between the modeled spiking rates in wt and tko SGNs. (A) An exemplary cumulative distribution function of inter-spike intervals of SGNs. Blue solid line – experimental data (wt), red dashed line – the best model fit. τ_R estimated by this model is likely a minor overestimate because this model ignores the finding that spiking slightly deviates from Poissonian statistics for short inter-spike intervals (1). (B) Dependence of the discrepancy between the experimental data and the model from (A) on the fitting parameter τ_R . As it follows from the expression of $P^M(t)$ given in Methods, the discrepancy measure has two equivalent minimum points. We found, however, that, in most of the cases considered, the minimum point corresponding to the larger of the two values of τ_R resulted in release rate estimates considerably higher than those based on the capacitance increment recordings from wt IHCs. We thus selected the smaller of the two τ_R estimates, which always gave reasonable release rate estimates. In a few cases, when both estimates of τ_R resulted in reasonable release rates, the difference between them was small. (C) Scatter plot of the overall refractory period estimate $t_A + \tau_R$ vs. steady-state spike rate from different SGNs (wt $n = 35$, tko $n = 87$). (D) Spike rate dependence on $t_A + \tau_R$ of modeled tko SGNs. Different colors represent spike rate estimates at different time points after stimulus onset. The scaling coefficient sc was chosen in such a way that the modeled spike rate of wt SGNs, derived from the ΔC_m data from wt IHCs, equaled the experimental observation – 250 Hz – at a given $t_A + \tau_R$, 50 ms after stimulus onset. The sc values increased from 0.23 at $t_A + \tau_R = 0$ to 0.94 at $t_A + \tau_R = 3$ ms. The same sc values were then used for calculating spike rates of modelled tko SGNs based on ΔC_m data from tko IHCs.

6 Supplementary Figure 6

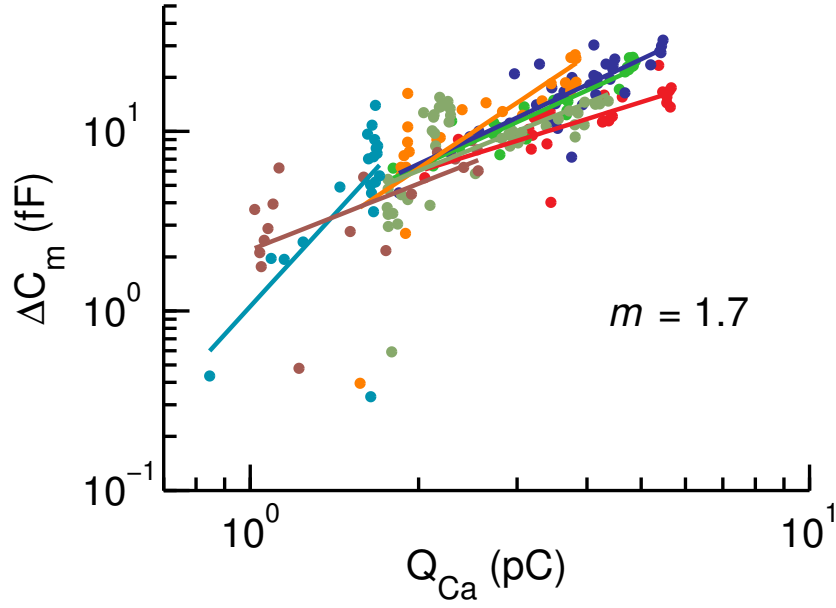


Figure S6: Apparent Ca^{2+} cooperativity of exocytosis in the operating range of Ca^{2+} influx at IHC synapses used for estimating the effective coupling distance R_c . Apparent Ca^{2+} cooperativities were estimated as the slope factors of linear fits (solid lines) of ΔC_m vs Q_{Ca} relations based on external $[\text{Ca}^{2+}]$ manipulation from seven mature IHCs (points) in log-log scale. Each color in the figure represents a particular cell. The data were taken from (2). Q_{Ca} interval used for the data fitting shown here was $[\max[Q_{Ca}]/2.5, \max[Q_{Ca}]]$ for each cell individually. The resulting Ca^{2+} cooperativity averaged over all cells, which we denote by m , was equal to 1.7. This value of m was used for estimating the effective coupling distance R_c , as described in Methods. To make sure that the estimate of m was not sensitive to small changes in the choice of the left boundary of the Q_{Ca} interval, we also considered values of the left boundary from $\max[Q_{Ca}]/1.1$ to $\max[Q_{Ca}]/3$. The resulting m values varied between 1.5 and 1.9.

7 Modeling of Ca^{2+} Dynamics (Including Supplementary Figures 7 – 11)

In this section, we provide additional information on modeling Ca^{2+} dynamics in the framework of a single Ca^{2+} source model formulated in Methods.

7.1 Reaction-Diffusion equations for $[\text{Ca}^{2+}]$ dynamics

In the presence of one of the mobile exogenous buffers, BAPTA or EGTA, the dynamics of $[\text{Ca}^{2+}]$ and concentrations of the mobile Ca^{2+} buffers following the onset of Ca^{2+} influx at $t = 0$ were modeled by the following closed system of reaction-diffusion equations:

$$\begin{cases} \partial_t[\text{MgB}_0] = k'_{\text{on},0} \cdot [\text{Mg}^{2+}] \cdot ([\text{B}_0]_{\text{T}} - [\text{MgB}_0] - [\text{CaB}_0]) - (k'_{\text{off},0} - D_0 \cdot \Delta_r) \cdot [\text{MgB}_0] \\ \partial_t[\text{Mg}^{2+}] = (D_0 \cdot \Delta_r[\text{MgB}_0] - \partial_t[\text{MgB}_0]) + D' \cdot \Delta_r[\text{Mg}^{2+}] \\ \partial_t[\text{CaB}_0] = k_{\text{on},0} \cdot [\text{Ca}^{2+}] \cdot ([\text{B}_0]_{\text{T}} - [\text{MgB}_0] - [\text{CaB}_0]) - (k_{\text{off},0} - D_0 \cdot \Delta_r) \cdot [\text{CaB}_0] \\ \partial_t[\text{CaB}_1] = k_{\text{on},1} \cdot [\text{Ca}^{2+}] \cdot ([\text{B}_1]_{\text{T}} - [\text{CaB}_1]) - (k_{\text{off},1} - D_1 \cdot \Delta_r) \cdot [\text{CaB}_1] \\ \partial_t[\text{Ca}^{2+}] = \sum_{i=0}^1 (D_i \cdot \Delta_r[\text{CaB}_i] - \partial_t[\text{CaB}_i]) + D \cdot \Delta_r[\text{Ca}^{2+}] \end{cases} .$$

Here, B_0 stands for ATP, and B_1 stands either for BAPTA or EGTA. k_{on} and k_{off} are Ca^{2+} binding and dissociation rates of a particular buffer. k'_{on} and k'_{off} are Mg^{2+} binding and dissociation rates of a particular buffer. D_0 and D_1 are the diffusion coefficients of B_0 and B_1 respectively. We assumed that the diffusion coefficients of Ca^{2+} - or Mg^{2+} -bound buffer molecules are equal to the diffusion coefficients of the corresponding free buffer molecules. D and D' stand for the diffusion coefficients of Ca^{2+} and Mg^{2+} respectively. $\Delta_r \equiv \frac{1}{r^2} \frac{\partial}{\partial r} (r^2 \frac{\partial}{\partial r} \dots)$ is the radial component of the Laplace operator. Note that concentrations of free buffer molecules at any point of space and time were determined by the difference between the total and Mg^{2+} -bound and/or Ca^{2+} -bound buffer concentrations. The total buffer concentrations were constant in space and time. This applies whenever Ca^{2+} -bound and Mg^{2+} -bound molecules have the same diffusion coefficients as the corresponding free buffer molecules, the total buffer concentrations are distributed uniformly within the simulation volume at $t = 0$ (as it was assumed in our model), and boundary conditions formulated in the next paragraph are used (see (3)).

In the case of the original model, the boundary conditions read as

$$\left. \frac{\partial[\text{Ca}^{2+}]}{\partial r} \right|_{r=r_0} = -\frac{i_{\text{Ca}}}{4 \cdot \pi \cdot D \cdot F \cdot r_0^2} \cdot H(t), \quad \left. \frac{\partial[X]}{\partial r} \right|_{r=r_0} = 0, \quad \left. \frac{\partial[\text{Ca}^{2+}]}{\partial r} \right|_{r=R} = 0, \quad \left. \frac{\partial[X]}{\partial r} \right|_{r=R} = 0,$$

here, X – Mg^{2+} or one of the Ca^{2+} or Mg^{2+} bound buffer molecules, F – Faraday constant, $H(t)$ – Heaviside step function. In the case of the modified version of the original model considered in section 7.6, the boundary conditions read as

$$\left. \frac{\partial[\text{Ca}^{2+}]}{\partial r} \right|_{r=r_0} = -\frac{i_{\text{Ca}}}{4 \cdot \pi \cdot D \cdot F \cdot r_0^2} \cdot H(t), \quad \left. \frac{\partial[X]}{\partial r} \right|_{r=r_0} = 0, \quad [\text{Ca}^{2+}]|_{r=R} = [\text{Ca}^{2+}]_0, \quad [X]|_{r=R} = [X]_0.$$

Here, $[\text{Ca}^{2+}]_0$ and $[X]_0$ are concentrations of Ca^{2+} and other ions and molecules in the simulation volume before onset of Ca^{2+} influx. Noteworthy, due to the symmetry, a hemispherical source model with

reflecting boundary at the base of the hemispherical simulation volume is equivalent to a spherical source model, with identical Ca^{2+} flux density, embedded in a spherical simulation volume.

In the presence of mobile endogenous Ca^{2+} buffers, $[\text{Ca}^{2+}]$ was determined by the following set of equations (or a particular subset of this set, when not all of the physiological endogenous buffers were considered together):

$$\left\{ \begin{array}{l} \partial_t[\text{MgB}_0] = k'_{\text{on},0} \cdot [\text{Mg}^{2+}] \cdot ([\text{B}_0]_{\text{T}} - [\text{MgB}_0] - [\text{CaB}_0]) - (k'_{\text{off},0} - D_0 \cdot \Delta_r) \cdot [\text{MgB}_0] \\ \partial_t[\text{MgB}_1] = k'_{\text{on},1} \cdot [\text{Mg}^{2+}] \cdot (2 \cdot [\text{B}_1]_{\text{T}} - [\text{MgB}_1] - [\text{CaB}_1]) - (k'_{\text{off},1} - D_1 \cdot \Delta_r) \cdot [\text{MgB}_1] \\ \partial_t[\text{Mg}^{2+}] = \sum_{i=0}^1 (D_i \cdot \Delta_r[\text{MgB}_i] - \partial_t[\text{MgB}_i]) + D' \cdot \Delta_r[\text{Mg}^{2+}] \\ \partial_t[\text{CaB}_0] = k_{\text{on},0} \cdot [\text{Ca}^{2+}] \cdot ([\text{B}_0]_{\text{T}} - [\text{MgB}_0] - [\text{CaB}_0]) - (k_{\text{off},0} - D_0 \cdot \Delta_r) \cdot [\text{CaB}_0] \\ \partial_t[\text{CaB}_1] = k_{\text{on},1} \cdot [\text{Ca}^{2+}] \cdot (2 \cdot [\text{B}_1]_{\text{T}} - [\text{MgB}_1] - [\text{CaB}_1]) - (k_{\text{off},1} - D_1 \cdot \Delta_r) \cdot [\text{CaB}_1] \\ \partial_t[\text{CaB}_2] = k_{\text{on},2} \cdot [\text{Ca}^{2+}] \cdot (4 \cdot [\text{B}_2]_{\text{T}} - [\text{CaB}_2]) - (k_{\text{off},2} - D_2 \cdot \Delta_r) \cdot [\text{CaB}_2] \\ \partial_t[\text{CaB}_3] = k_{\text{on},3} \cdot [\text{Ca}^{2+}] \cdot ([\text{B}_3]_{\text{T}} - [\text{CaB}_3]) - (k_{\text{off},3} - D_3 \cdot \Delta_r) \cdot [\text{CaB}_3] \\ \partial_t[\text{CaB}_4] = k_{\text{on},4}^{\text{T}} \cdot [\text{Ca}^{2+}] \cdot (2 \cdot [\text{B}_4]_{\text{T}} - [\text{CaB}_4] - [\text{Ca}_2\text{B}_4]) - (k_{\text{off},4}^{\text{T}} - D_4 \cdot \Delta_r) \cdot [\text{CaB}_4] \\ \partial_t[\text{Ca}_2\text{B}_4] = k_{\text{on},4}^{\text{R}} \cdot [\text{Ca}^{2+}] \cdot [\text{CaB}_4] - (k_{\text{off},4}^{\text{R}} - D_4 \cdot \Delta_r) \cdot [\text{Ca}_2\text{B}_4] \\ \partial_t[\text{Ca}^{2+}] = \sum_{i=0}^3 (D_i \cdot \Delta_r[\text{CaB}_i] - \partial_t[\text{CaB}_i]) + D_i \cdot \Delta_r[\text{Ca}_2\text{B}_4] - \partial_t[\text{Ca}_2\text{B}_4] + D \cdot \Delta_r[\text{Ca}^{2+}] \end{array} \right. .$$

Here, B_0 stands for ATP, B_1 – parvalbumin- α (PV), B_2 – calbindin-D28k (CB), B_3 – non-cooperative binding site of calretinin ($\text{CR}_{\text{non.coop.}}$), B_4 – cooperative binding site of calretinin with no Ca^{2+} -bound ($\text{CR}_{\text{coop.}}$), CaB_4 – cooperative binding site of calretinin with one Ca^{2+} -bound ($\text{CaCR}_{\text{coop.}}$), Ca_2B_4 – cooperative binding site of calretinin with two Ca^{2+} bound. The following Ca^{2+} and Mg^{2+} binding and unbinding rates were used for simulations:

- BAPTA – $k_{\text{on}} = 400 \text{ mM}^{-1} \cdot \text{ms}^{-1}$, $k_{\text{off}} = 0.088 \text{ ms}^{-1}$, (3).
- EGTA – $k_{\text{on}} = 10 \text{ mM}^{-1} \cdot \text{ms}^{-1}$, $k_{\text{off}} = 0.0007 \text{ ms}^{-1}$, (4).
- ATP – $k_{\text{on}} = 1000 \text{ mM}^{-1} \cdot \text{ms}^{-1}$, $k_{\text{off}} = 90 \text{ ms}^{-1}$, (5).
- ATP (Mg^{2+}) – $k_{\text{on}} = 10 \text{ mM}^{-1} \cdot \text{ms}^{-1}$, $k_{\text{off}} = 0.45 \text{ ms}^{-1}$, (5).
- PV – $k_{\text{on}} = 103 \text{ mM}^{-1} \cdot \text{ms}^{-1}$, $k_{\text{off}} = 0.00095 \text{ ms}^{-1}$, (6).
- PV (Mg^{2+}) – $k_{\text{on}} = 0.8 \text{ mM}^{-1} \cdot \text{ms}^{-1}$, $k_{\text{off}} = 0.025 \text{ ms}^{-1}$, (6).
- CB – $k_{\text{on}} = 75 \text{ mM}^{-1} \cdot \text{ms}^{-1}$, $k_{\text{off}} = 0.0295 \text{ ms}^{-1}$, (7).
- $\text{CR}_{\text{non.coop.}}$ – $k_{\text{on}} = 7.3 \text{ mM}^{-1} \cdot \text{ms}^{-1}$, $k_{\text{off}} = 0.252 \text{ ms}^{-1}$, (8).
- $\text{CR}_{\text{coop.}}$ – $k_{\text{on}} = 1.8 \text{ mM}^{-1} \cdot \text{ms}^{-1}$, $k_{\text{off}} = 0.053 \text{ ms}^{-1}$, (8).
- $\text{CaCR}_{\text{coop.}}$ – $k_{\text{on}} = 310 \text{ mM}^{-1} \cdot \text{ms}^{-1}$, $k_{\text{off}} = 0.02 \text{ ms}^{-1}$, (8).

The diffusion coefficients were set to $0.22 \mu\text{m}^2 \cdot \text{ms}^{-1}$ for Ca^{2+} , Mg^{2+} , ATP, BAPTA, and EGTA (3), to $0.02 \mu\text{m}^2 \cdot \text{ms}^{-1}$ for PV and CR (8,9), and to $0.043 \mu\text{m}^2 \cdot \text{ms}^{-1}$ for CB (10). The resting Ca^{2+} concentration, $[\text{Ca}^{2+}](r, t = 0)$, was set to 50 nM (11).

The above systems of partial differential equations were solved numerically in MATLAB using built-in PDE solver *pdepe*.

7.2 Temporal evolution of $[Ca^{2+}]$

Fig. S7A-B show time evolution of normalized $[Ca^{2+}]$ after onset of stimulus¹ at distances up to 100 nm from the edge of a $r_0 = 1$ nm hemispherical source ($i_{Ca} = 15$ pA) embedded in a hemispherical simulation volume of $2\text{ }\mu\text{m}$ radius with reflecting boundary conditions. In all plots shown, $[Ca^{2+}](r, t)$ was normalized to $[Ca^{2+}](r, t = 20\text{ ms})$. Panels on the left in **Fig. S7** were obtained for the simulation volume filled with 2 mM MgATP, while panels on the right correspond to the simulation volume filled with 2 mM MgATP + 0.5 mM BAPTA. It follows from the panels (A) and (B) that the temporal profiles of $[Ca^{2+}]$ were approximately characterized by two time scales. The initial time scale corresponded to the quasi-equilibration of Ca^{2+} diffusion and reaction with the buffer molecules. The later, much slower time scale corresponded to accumulation of Ca^{2+} and the accompanying increase in the fraction of Ca^{2+} -bound buffer molecules due to the prolonged Ca^{2+} influx. As can be seen in the plots, $[Ca^{2+}]$ at distances up to 100 nm away from the source stayed rather constant during the first 20 ms after the initial build-up. This was especially true for points located closer to the source. At $t = 100$ ms, however, the accumulation of Ca^{2+} was considerable at the greater distances, in relative terms. This is seen better in **Fig. S7C-D**, where normalized spatial $[Ca^{2+}]$ profiles are shown for selected time points².

In the case of a real presynaptic active zone, a 15 pA influx of Ca^{2+} ions (a finding of our present work) is spread over an area of the cellular membrane which is considerably larger than the surface area of a $r_0 = 1$ nm hemispherical source. Thus, the absolute levels of $[Ca^{2+}]$ at small distances from the source were overestimated in our model³. This overestimation could result in a decreased effect of the accumulated bulk Ca^{2+} on $[Ca^{2+}]$ in the proximity of the source during prolonged depolarizations. To examine this, we repeated the calculations with a $r_0 = 70$ nm radius hemispherical source. The surface area of this larger hemisphere approximately matched the area of the presynaptic density at IHC synapses ($420 \times 80\text{ nm}^2$, (2)). We found that, although the influence of the accumulated Ca^{2+} on $[Ca^{2+}]$ was slightly stronger in this case, the conclusions drawn from the model with $r_0 = 1$ nm radius hemispherical source did not change – compare plots in **Fig. S7E-F** with the corresponding plots in **Fig. S7A-B**. Note that, when a point of interest is close to the edge of the Ca^{2+} source, the average distance between the point of interest and effective Ca^{2+} point sources which are spread on the surface of the hemisphere is considerably higher in the case of the $r_0 = 70$ nm radius hemisphere than the $r_0 = 1$ nm radius hemisphere. This is one of the reasons why the influence of the accumulated Ca^{2+} on $[Ca^{2+}]$ was slightly stronger for the $r_0 = 70$ nm source than for the $r_0 = 1$ nm source. The same fact explains why initial phases of the $[Ca^{2+}]$ temporal profiles were associated with a slightly slower time scale in the case of the larger, $r_0 = 70$ nm, hemisphere.

¹“Onset of stimulus” and “onset of Ca^{2+} influx” are used as synonyms in sections 6.1 - 6.6.

²Similar effects were also found when 2 mM MgATP + 1 mM BAPTA or 2 mM MgATP + (0.5 – 1) mM EGTA were used as Ca^{2+} buffers. Naturally, the effect of Ca^{2+} accumulation on $[Ca^{2+}]$ is less pronounced for higher concentrations of exogenous Ca^{2+} buffers and/or smaller i_{Ca} levels.

³Note that, in this work, estimations of concentrations of the endogenous buffers or the coupling distance between presynaptic Ca^{2+} channels and Ca^{2+} sensors of exocytosis were based on the ratios of $[Ca^{2+}]$ estimated in different Ca^{2+} buffering conditions, not the absolute levels of $[Ca^{2+}]$.

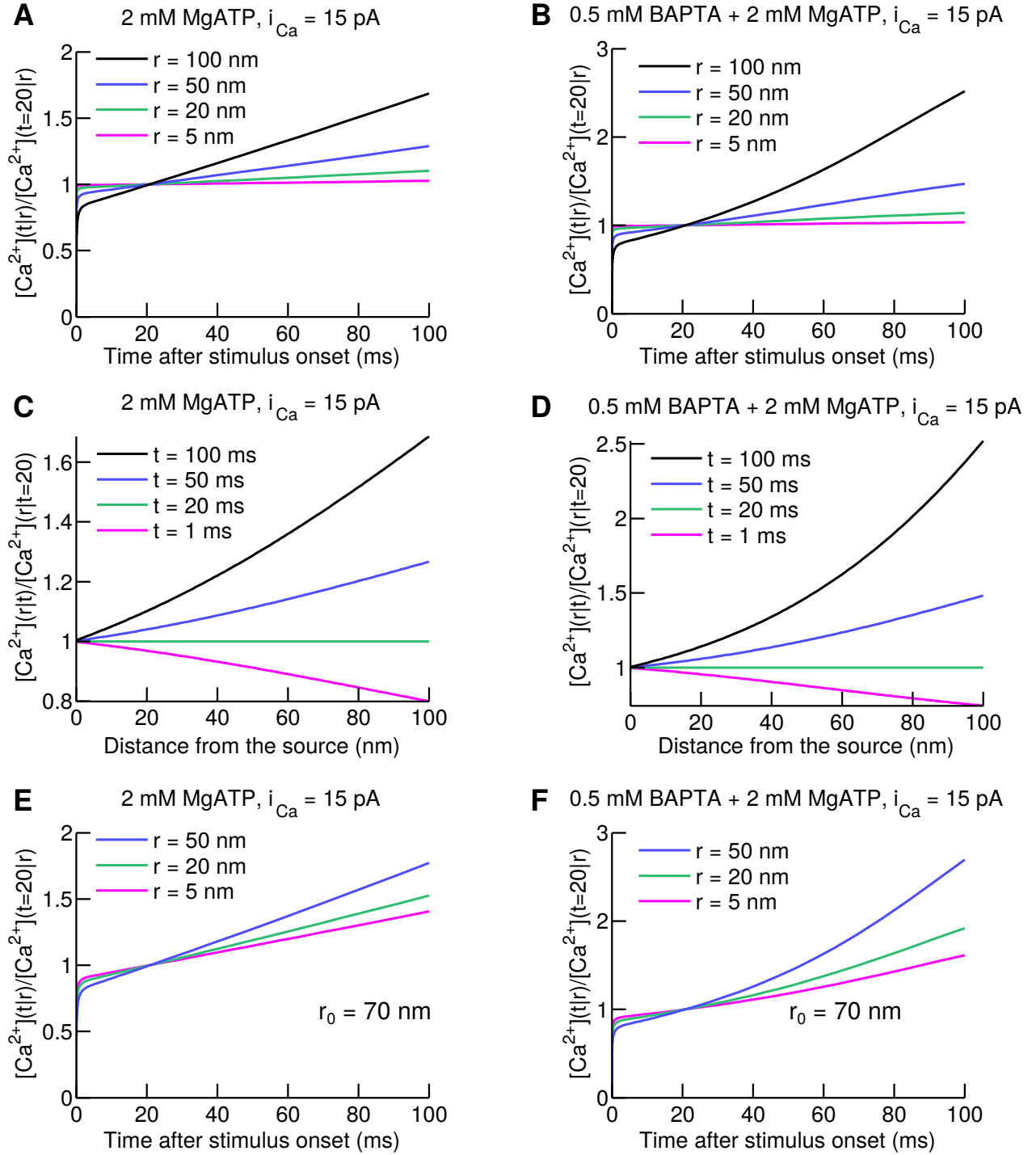


Figure S7: Temporal evolution of $[Ca^{2+}]$. (A) Ratios of temporal $[Ca^{2+}]$ profiles at certain distances from the source, $[Ca^{2+}](t|r)/[Ca^{2+}](t=20|r)$, based on $i_{Ca} = 15$ pA Ca^{2+} influx through a $r_0 = 1$ nm hemispherical source with the simulation volume filled with 2 mM MgATP. (B) The same as (A), but with the simulation volume filled with 0.5 mM BAPTA and 2 mM MgATP. (C) Ratios of spatial Ca^{2+} profiles at fixed times, $[Ca^{2+}](r|t)/[Ca^{2+}](r|t=20)$, corresponding to the temporal profiles shown in (A). (D) The same as (C), but with the simulation volume filled with 0.5 mM BAPTA and 2 mM MgATP. (E) Temporal profiles of $[Ca^{2+}]$ based on $i_{Ca} = 15$ pA Ca^{2+} influx through a $r_0 = 70$ nm hemispherical source with simulation volume filled with 2 mM MgATP. (F) The same as (E), but with the simulation volume filled with 0.5 mM BAPTA and 2 mM MgATP.

7.3 Extent of Ca^{2+} buffer depletion due to Ca^{2+} influx

To find the value of i_{Ca} which results in a similar extent of Ca^{2+} buffer depletion for a $r_0 = 1$ nm hemispherical source as at the presynaptic active zone, we varied levels of i_{Ca} and compared the resulting Ca^{2+} buffer concentrations with the ones corresponding to a $r_0 = 70$ nm source⁴ with $i_{\text{Ca}} = 15$ pA. **Fig. S8** shows the ratios of increments of the Ca^{2+} -bound buffer concentrations due to onset of Ca^{2+} influx through the $r_0 = 1$ nm and $r_0 = 70$ nm hemispherical sources as functions of the distance from the edge of the sources. In the case shown here, Ca^{2+} influx was set to 15 pA for the $r_0 = 70$ nm source and 7 pA for the $r_0 = 1$ nm source. The concentrations were estimated 20 ms after onset of Ca^{2+} influx. The simulation volume was a hemisphere of $2\text{ }\mu\text{m}$ radius with reflecting boundary conditions. The total concentrations of exogenous buffers BAPTA and EGTA, each of them considered separately, were set to either 0.5 mM or 1 mM. Moreover, in all considered cases, a total of 2 mM ATP was included. As can be seen from the plots, the ratios of the amounts of depleted buffers, BAPTA + ATP or EGTA + ATP, were around 1 or higher for the distances considered. This indicates that the $r_0 = 1$ nm source with $i_{\text{Ca}} = 7$ pA resulted in a similar extent of Ca^{2+} buffer depletion as the $r_0 = 70$ nm source with $i_{\text{Ca}} = 15$ pA over distances 0 to 50 nm from the Ca^{2+} source.

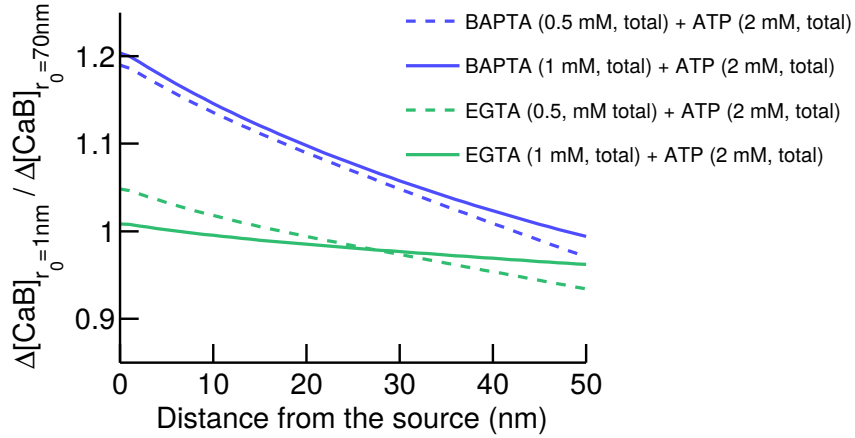


Figure S8: Ratios between increased Ca^{2+} -bound buffer concentrations due to Ca^{2+} influx for hemispherical Ca^{2+} sources with $r_0 = 1$ nm, $i_{\text{Ca}} = 7$ pA, and $r_0 = 70$ nm, $i_{\text{Ca}} = 15$ pA as functions of the distance from the edge of the sources.

7.4 Influence of the partial buffer depletion on the $[\text{Ca}^{2+}]$ vs. i_{Ca} relation

It was assumed in the model considered in Results that integrated exocytosis, ΔC_m follows $[\text{Ca}^{2+}]$ at the sensor of exocytosis according to a power law relation. However, $[\text{Ca}^{2+}]$ at the sensor of exocytosis is not an experimentally accessible quantity currently. Thus, in order to determine the exponent parameter of the relation between ΔC_m and $[\text{Ca}^{2+}]$ at the sensor of exocytosis, we have to employ the experimentally accessible relation between the integrated release and integrated Ca^{2+} influx, Q_{Ca} : $\Delta C_m \sim (Q_{\text{Ca}})^m$ (see section 6). We show below that $Q_{\text{Ca}} \sim [\text{Ca}^{2+}]^q$. Thus, $\Delta C_m \sim [\text{Ca}^{2+}]^{m \cdot q}$.

Due to nonlinearities inherent to the dynamics of Ca^{2+} and buffer concentrations, the dependence of $[\text{Ca}^{2+}](t, r)$ on the Ca^{2+} influx level i_{Ca} is nonlinear in general. We simulated the dependence of

⁴Which has the surface area similar in extent to that of a real IHC presynaptic density as explained in section 7.2.

$[\text{Ca}^{2+}](t, r)$ on i_{Ca} to quantitatively check how much this relation deviates from the linear approximation. It turned out that, for all the considered buffering conditions, the relation was well approximated by $[\text{Ca}^{2+}](r) \sim i_{\text{Ca}}^{1/q(r)}$ at distances of 0 to 100 nm from the source. **Fig. S9B-D** show the $[\text{Ca}^{2+}]$ vs. i_{Ca} relations at distances of 0, 10, 25, 50, 100 nm away from the source, at $t = 20$ ms for three different Ca^{2+} buffer sets: 2 mM MgATP, 0.5 mM BAPTA + 2 mM MgATP, 0.5 mM EGTA + 2 mM MgATP. Black solid lines represent the simulated data, while magenta dashed lines represent the best fits of the form $[\text{Ca}^{2+}](r) = k(r) \cdot i_{\text{Ca}}^{1/q(r)}$. i_{Ca} values ranging from 0.3 pA to 7 pA were considered. The radius of the hemispherical source was set to 1 nm. The radius of the simulation volume hemisphere was $2 \mu\text{m}$. The boundary was reflective for all ions and molecules considered. **Fig. S9A** shows the dependence of the exponent q on the distance from the source, r , for the three aforementioned Ca^{2+} buffering conditions. q values were only slightly smaller than 1, thus the $[\text{Ca}^{2+}]$ vs. i_{Ca} relation was only slightly supralinear. When concentrations of BAPTA and EGTA were increased from 0.5 mM to 1 mM, $q(r)$ shifted slightly towards 1.

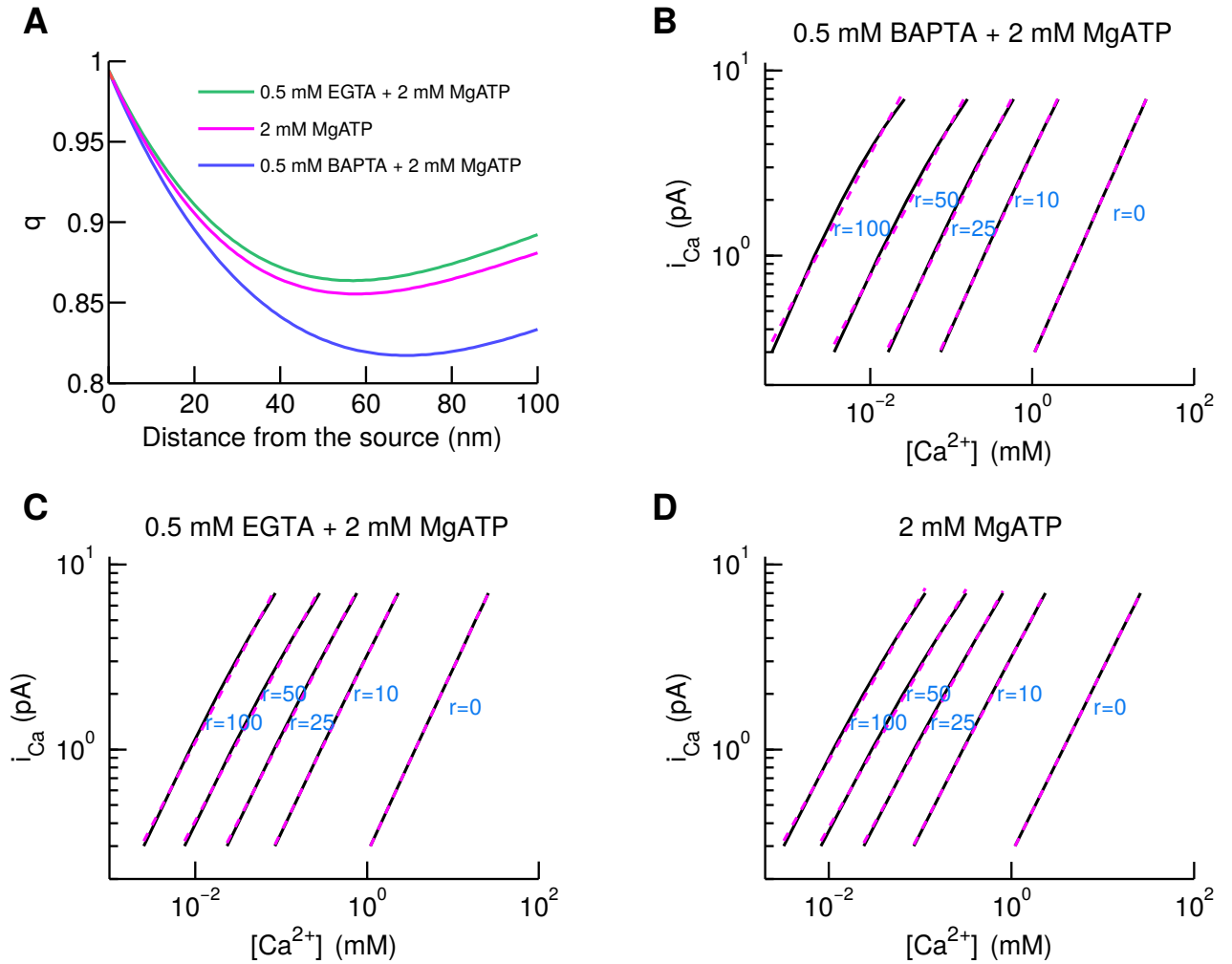


Figure S9: Influence of the partial buffer depletion on $[\text{Ca}^{2+}]$ vs. i_{Ca} relation. (A) Dependence of the exponent q corresponding to the best fits of simulated i_{Ca} vs. $[\text{Ca}^{2+}]$ relations by $i_{\text{Ca}} = k \cdot [\text{Ca}^{2+}]^q$ on the distance from a $r_0 = 1$ nm hemispherical Ca^{2+} source with $i_{\text{Ca}} = 7$ pA. (B-D) Simulated i_{Ca} vs. $[\text{Ca}^{2+}]$ relations (black solid lines) and the optimal fits of the form $i_{\text{Ca}} = k \cdot [\text{Ca}^{2+}]^q$ (dashed magenta lines) with different contents of Ca^{2+} buffers.

Note that $Q_{Ca} = t \cdot i_{Ca}$ for constant i_{Ca} , where t is the time passed since stimulus onset. Thus, $[Ca^{2+}](r) = (k(r)/t^{1/q(r)}) \cdot Q_{Ca}^{1/q(r)}$. To take into account the effect of partial buffer depletion on the estimate of the effective coupling distance between presynaptic Ca^{2+} channels and Ca^{2+} sensors of exocytosis for $i_{Ca} = 7$ pA, we used $q(r)$ profiles corresponding to 0.5 mM BAPTA + 2 mM MgATP buffering conditions, which roughly approximates the natural Ca^{2+} buffering conditions in IHC as shown in our present work. We used $q(r) \equiv 1$ for estimating the coupling distance for weak $[Ca^{2+}]$ influx ($i_{Ca} = 0.3$ pA).

7.5 Effect of accumulated bulk Ca^{2+} during prolonged stimulation on the model predictions of concentrations of the endogenous Ca^{2+} buffers

The upper bounds for concentrations of the endogenous Ca^{2+} buffers shown in **Fig. 9C** were estimated by probing $[Ca^{2+}]$ at $t = 100$ ms after stimulus onset. It was shown in section 7.2 (see **Fig. S7A-B**) that the effect of the accumulated Ca^{2+} on $[Ca^{2+}]$ increased with time after stimulus onset from negligible at $t = 20$ ms to significant at $t = 100$ ms. This could affect the estimates of the upper bounds for the concentrations of the endogenous Ca^{2+} buffers, which were determined by matching the spatial $[Ca^{2+}]$ profiles at $t = 100$ ms (see Results and **Fig. 9C**). To test this, we re-estimated the upper bounds for the concentrations of the endogenous Ca^{2+} buffers by probing spatial profiles of $[Ca^{2+}]$ at times between 20 ms and 100 ms after stimulus onset. Solid lines in **Fig. S10** show dependencies of the estimates of Ca^{2+} -binding site concentrations of the endogenous buffers on the time when $[Ca^{2+}]$ was probed. The estimates of Ca^{2+} -binding site concentrations for calbindin-D28k and parvalbumin- α decreased only slightly when comparing values obtained at $t = 20$ ms to $t = 100$ ms: from 6.4 mM to 5.2 mM for calbindin-D28k and from 5.0 mM to 4.2 mM for parvalbumin- α . The difference was more significant for calretinin – the estimate of the Ca^{2+} -binding site concentration decreased from 21.0 mM at $t = 20$ ms to 13.8 mM at $t = 100$ ms. The reason why calretinin was so sensitive to the accumulated Ca^{2+} is that it has highly cooperative Ca^{2+} binding sites, with the first binding step being much slower than the second one.

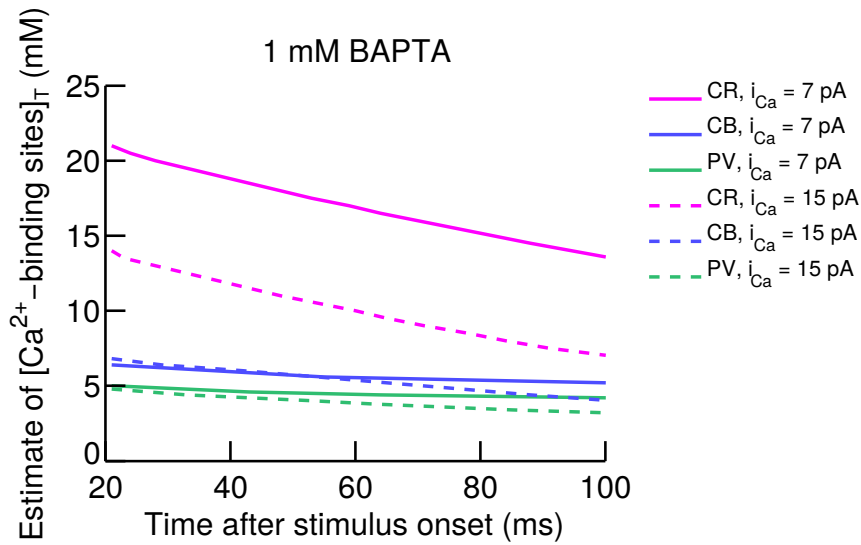


Figure S10: Estimation of concentrations of the endogenous buffer Ca^{2+} -binding sites equivalent to 1 mM BAPTA based on $[Ca^{2+}]$ probed at different moments after stimulus onset.

Dashed lines in **Fig. S10** show dependencies of the estimates of the Ca^{2+} -binding site concentrations on the moment when $[\text{Ca}^{2+}]$ was probed after onset of i_{Ca} of 15 pA. The results were essentially the same as with $i_{\text{Ca}} = 7$ pA for calbindin-D28k and parvalbumin- α . However, the concentration estimates were decreased by ~ 7 mM for calretinin.

7.6 Influence of the type of boundary conditions on the estimates of the endogenous buffer concentrations and the coupling distance R_c

The original model of $[\text{Ca}^{2+}]$ dynamics presented in this work assumed a hemispherical simulation volume with $2\ \mu\text{m}$ radius. The boundaries of the simulation volume were set to be reflective to all molecules and ions considered. The choice of the radius of the simulation volume was based on the finding that the presynaptic active zones of inner hair cells are separated by $2\ \mu\text{m}$ on average (12). The reflecting boundary condition set at the hemispherical boundary of the simulation volume was meant to effectively take into account accumulation of Ca^{2+} due to Ca^{2+} channels from the synapse under consideration as well as Ca^{2+} channels from neighboring synapses. On the other hand, such a boundary condition could lead to an overestimation of the $[\text{Ca}^{2+}]$ because it does not take into account removal of Ca^{2+} ions and Ca^{2+} -bound buffer molecules from the neighborhood of the presynaptic site due to exchange of the molecules with the large non-synaptic part of the IHC volume. Indeed, 12 hemispheres with $2\ \mu\text{m}$ radius correspond to only one percent of hair cell volume ($2.2 \cdot 10^{-15}\ \text{m}^{-3}$, (13)) on average. The purely reflective boundary at the base of the simulation volume ignores Ca^{2+} removal by Ca^{2+} pumps. To check how the choice of the boundary conditions affected our estimates of the endogenous buffer concentrations and the coupling distance between presynaptic Ca^{2+} channels and Ca^{2+} sensors of exocytosis, we performed equivalent simulations with different boundary conditions. Specifically, we fixed concentrations of all considered molecules and ions at the hemispherical boundary of the simulation volume to their resting levels, i.e., levels before the onset of Ca^{2+} influx. The base of the hemisphere was chosen to be reflecting as in the original model. The radius of the hemispherical simulation volume, R , was set to either $2\ \mu\text{m}$ or $4\ \mu\text{m}$. Such boundary conditions can be treated as overestimating the intensity of Ca^{2+} removal from the neighborhood of the presynaptic active zones.

Fig. S11A-B show plots of ratios $[\text{Ca}^{2+}](r|t)/[\text{Ca}^{2+}]^*(r|+\infty)$ at selected times. Here, $[\text{Ca}^{2+}](r|t)$ stands for $[\text{Ca}^{2+}]$ at the distance r from the source at moment t after stimulus onset, estimated by using the original model with reflecting boundary conditions. $[\text{Ca}^{2+}]^*(r|+\infty)$ stands for the steady state $[\text{Ca}^{2+}]$ at the distance r from the source, estimated by using the “resting-level” boundary conditions introduced in the previous paragraph (see also section 7.1). Solid (dashed) lines correspond to $[\text{Ca}^{2+}]^*$ estimated using a $R = 2\ \mu\text{m}$ ($R = 4\ \mu\text{m}$) simulation volume. **Fig. S11A** corresponds to 2 mM MgATP, **Fig. S11B** corresponds to 0.5 mM BAPTA + 2 mM MgATP. These profiles are quantitatively similar to the spatial profiles shown in **Fig. S7C-D**, where $[\text{Ca}^{2+}](r|t = 20)$ was used for scaling. The differences between the results corresponding to $R = 2\ \mu\text{m}$ and $R = 4\ \mu\text{m}$ simulation volumes were negligible (compare solid and dashed lines in **Fig. S11A-B**). This similarity can be explained by the fact that, in the first 20 ms after onset of Ca^{2+} influx, the processes of Ca^{2+} diffusion and binding to the buffers were confined to a small volume, which was far away from the hemispherical surface of the simulation volume. These results suggest that the estimate of R_c is rather insensitive to the precise choice of boundary conditions, given

that the radius of the simulation volume, R , is $\geq 2 \mu\text{m}$. This idea is corroborated by the observation that dependencies of the discrepancy measure z on the effective distance between the Ca^{2+} source and Ca^{2+} sensors of exocytosis shown in **Fig. S11C** were strikingly similar to the equivalent plots shown in **Fig. 9B**. Estimates of the effective concentrations of the endogenous buffer Ca^{2+} binding sites did not strongly depend on which of the boundary conditions were used either (compare **Fig. S11D** with **Fig. 9C**), except the upper bound estimate for calretinin. The latter was larger by $\sim 50\%$ in the case of the resting-level boundary conditions because of the Ca^{2+} binding cooperativity of calretinin.

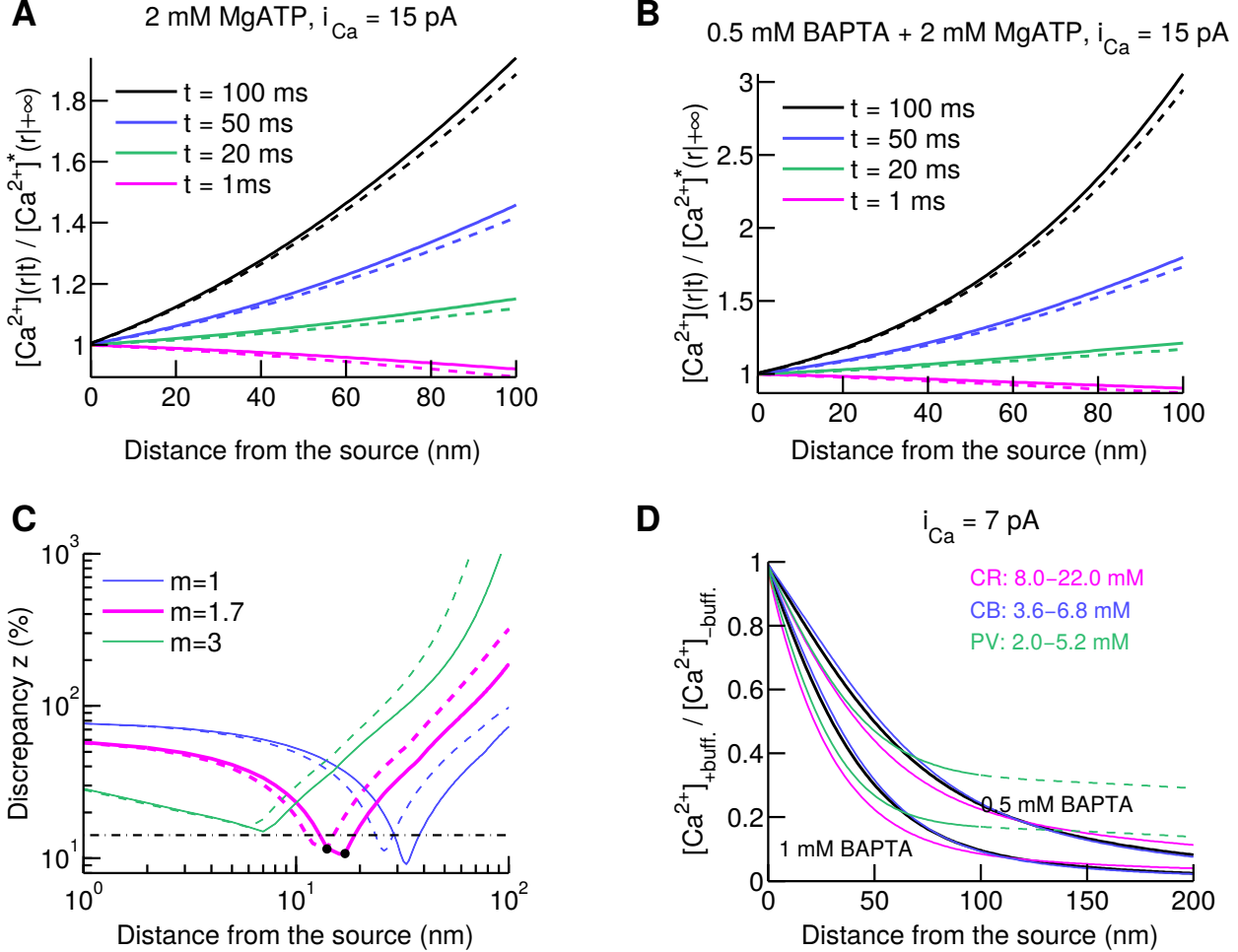


Figure S11: Results based on the simulations with boundary conditions that fix concentrations of all molecular species to the resting levels at the hemispherical surface of the simulation volume. (A-B) Spatial profiles of ratios $[\text{Ca}^{2+}](r|t) / [\text{Ca}^{2+}](r|+\infty)$ at selected times. Solid (dashed) lines correspond to $[\text{Ca}^{2+}](r|+\infty)$ estimated with the radius of the simulation volume equal to $R = 2 \mu\text{m}$ ($R = 4 \mu\text{m}$). (C) Dependence of the discrepancy measure z on the effective coupling distance between presynaptic Ca^{2+} channels and sensors of exocytosis. Dashed lines correspond to $i_{\text{Ca}} = 0.3 \text{ pA}$, solid lines correspond to $i_{\text{Ca}} = 7 \text{ pA}$. The black dash-dotted line corresponds to the average of the experimental s.e.m. $[\Delta C_m] / \langle \Delta C_m \rangle$ over different Ca^{2+} buffering conditions ($R = 2 \mu\text{m}$). (D) Ratios of $[\text{Ca}^{2+}]$ in the presence, denoted by $[\text{Ca}^{2+}]_{+\text{buff.}}$, and the absence, denoted by $[\text{Ca}^{2+}]_{-\text{buff.}}$, of particular buffers as functions of the distance from the 1 nm radius hemispherical source. Color lines are the best fits of $[\text{Ca}^{2+}]_{+\text{buff.}} / [\text{Ca}^{2+}]_{-\text{buff.}}$ corresponding to 0.5 mM and 1 mM BAPTA with $[\text{Ca}^{2+}]_{+\text{buff.}} / [\text{Ca}^{2+}]_{-\text{buff.}}$ corresponding to either calretinin (magenta), calbindin-D28k (blue) or parvalbumin- α (green).

8 Defining and Evaluating the Effective Coupling Distance R_c (Including Supplementary Figure 12)

Several versions of the model of a single effective vesicular release site driven by a single effective Ca^{2+} channel have been applied to evaluate the proximity between presynaptic Ca^{2+} channels and Ca^{2+} sensors of exocytosis based on the differential effect of mobile exogenous Ca^{2+} buffers with different Ca^{2+} binding kinetics and concentrations on exocytosis (see, for example, (14 – 17)). Intuitively, the coupling distance, which we denote by R_c , estimated in the framework of that model reflects the proximity between the Ca^{2+} channels and the vesicular release sites within the active zone. However, how R_c is quantitatively related to the parameters which define the spatial arrangement of presynaptic Ca^{2+} channels and vesicular release sites, as well as the kinetic parameters which define the Ca^{2+} dynamics, has not been analyzed before.

In this section we provide a mathematical analysis for understanding the physical meaning of R_c . This analysis unravels that R_c , in general, is a complicated, nonlinear average of the physical distances between the presynaptic Ca^{2+} channels and Ca^{2+} sensors of exocytosis. The main advantage of the single Ca^{2+} source model compared to spatially resolved models is that it produces a single output, R_c , which embodies the essence of all possible active zone topographies which are compatible with the experimental data. However, as we explain later in this section, the model also has a disadvantage that the exact value of R_c depends not only on the structural but also on the kinetic parameters of the system, such as Ca^{2+} cooperativity of exocytosis or Ca^{2+} binding kinetics of intracellular Ca^{2+} buffers. Thus, to avoid misinterpretations of R_c , care has to be taken when designing the experiments.

In this section, we also provide results of spatially resolved models of IHC presynaptic active zones introduced previously (see (2)). We show that active zone topographies suggested as corresponding to the “ Ca^{2+} nanodomain coupling” regime in (2) are compatible with the R_c estimate determined in our present work.

8.1 Active zones with 1 vesicular release site and N Ca^{2+} channels, no Ca^{2+} buffers

First of all, let us consider a presynaptic active zone which contains N Ca^{2+} channels and one vesicular release site (see **Fig. S12A**). We assume that no Ca^{2+} buffers are present in the cytoplasm and that Ca^{2+} diffuses freely above the reflective cellular membrane. In this case, a particular channel i results in an increment of $[\text{Ca}^{2+}]$, which, averaged over time in steady state at fixed membrane potential, is inversely proportional to the distance from the mouth of that channel⁵ (3):

$$\delta\langle[\text{Ca}^{2+}]\rangle_i = \frac{i_{Ca} \cdot P_o}{4 \cdot \pi \cdot F \cdot D \cdot R_i}, \quad [1]$$

⁵For the sake of mathematical tractability, here and further on in sections 8.1 – 8.5, we treat Ca^{2+} channels as point sources and assume open boundary conditions above the plane of the plasma membrane (see (3)), unless stated otherwise. It follows from the results of section 7.6 that such an approximation would have negligible effect on the estimates of the effective coupling distance R_c .

where i_{Ca} is single Ca^{2+} channel current, R_i — distance from the mouth of i -th channel to the point of interest, F — Faraday constant, D — diffusion coefficient of Ca^{2+} , P_o — open probability of the channels in steady state at a given membrane potential. Let us now consider a response of such a model synapse to a depolarizing pulse of certain length. We assume that exocytosis at the synapse is fully determined by the time-averaged Ca^{2+} concentration at the vesicular release site⁶, $\langle[\text{Ca}^{2+}]\rangle = \sum_{i=1}^N \delta\langle[\text{Ca}^{2+}]\rangle_i$ ⁷, and is not affected by momentary Ca^{2+} concentration fluctuations due to the channel opening and closing (the validity of this assumption is considered in section 8.5). We also assume that functional relation between $\langle[\text{Ca}^{2+}]\rangle$ and the amount of vesicles released in a chosen time period T , which we denote by $\Delta_{rel.}$, is bijective: $\Delta_{rel.} = f(\langle[\text{Ca}^{2+}]\rangle)$. Given this, we can apply a single Ca^{2+} source model to determine the effective coupling distance R_c from a measured $\Delta_{rel.}$: R_c is the distance from a single Ca^{2+} source, with total Ca^{2+} influx $I_{Ca} = N \cdot i_{Ca}$, to the point of interest at which Ca^{2+} concentration is equal to $\langle[\text{Ca}^{2+}]\rangle = f^{-1}(\Delta_{rel.})$. Taking into account equation [1], we can express R_c in the following way:

$$\begin{aligned} R_c &= \frac{I_{Ca} \cdot P_o}{4 \cdot \pi \cdot F \cdot D \cdot \langle[\text{Ca}^{2+}]\rangle} = \frac{\sum_{i=1}^N (i_{Ca} \cdot P_o) / (4 \cdot \pi \cdot F \cdot D)}{\langle[\text{Ca}^{2+}]\rangle} = \frac{\sum_{i=1}^N R_i \cdot \delta\langle[\text{Ca}^{2+}]\rangle_i}{\langle[\text{Ca}^{2+}]\rangle} = \\ &= \sum_{i=1}^N R_i \cdot \left(\frac{\delta\langle[\text{Ca}^{2+}]\rangle_i}{\sum_{j=1}^N \delta\langle[\text{Ca}^{2+}]\rangle_j} \right) \equiv \langle R \rangle_{Ca}^{\mathcal{L}} \end{aligned} \quad [2]$$

Thus, R_c is a weighted average of distances from all the channels to the Ca^{2+} sensor of exocytosis, which we denote by $\langle R \rangle_{Ca}^{\mathcal{L}}$. Here, superscript \mathcal{L} stands for “linear” and subscript Ca indicates that the averaging weights depend on how $\delta\langle[\text{Ca}^{2+}]\rangle_i$ depends on R_i ⁸. The weight for each channel is the relative contribution of that channel to $\langle[\text{Ca}^{2+}]\rangle$ at the vesicular release site. The higher is the contribution of a channel to $\langle[\text{Ca}^{2+}]\rangle$ and, thus, exocytosis, the closer is $\langle R \rangle_{Ca}^{\mathcal{L}}$ to the distance from that channel to the sensor. Note that the choice $I_{Ca} = N \cdot i_{Ca}$ is derived from the requirement that $R_c = R_i$ when $R_i = R_j$ for any i and j , i.e., when all the channels are equidistant to the Ca^{2+} sensor.

⁶Here and further on, we assume that the exocytosis rate depends on $[\text{Ca}^{2+}]$ at a particular point associated with the vesicular release site which we will call “ Ca^{2+} sensor”. “ Ca^{2+} concentration at a vesicular release site” and “ Ca^{2+} concentration at a Ca^{2+} sensor of exocytosis” are used as synonyms in sections 8.1 – 8.5.

⁷Here and further on, we assume that the contribution of the background $[\text{Ca}^{2+}]$, i.e., $[\text{Ca}^{2+}]$ in the absence of stimulus, is negligible.

⁸It is shown in section 8.4 that, in general, the averaging weights depend not only on the quantitative expression of $\delta\langle[\text{Ca}^{2+}]\rangle_i$ vs. R_i but also on the properties of release rate dependence on $\langle[\text{Ca}^{2+}]\rangle$. Moreover, as it is shown in 8.2, the averaging is nonlinear if Ca^{2+} buffers are present in the presynaptic solution.

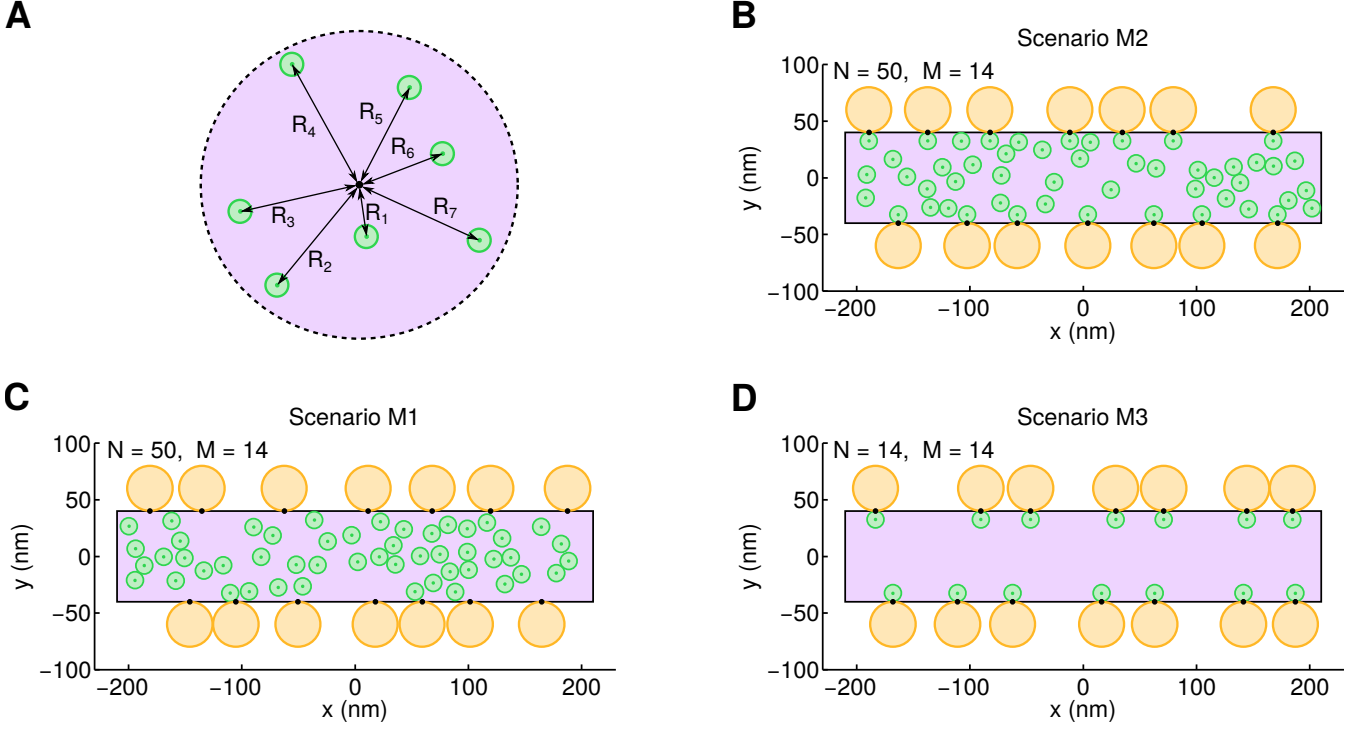


Figure S12: Examples of the active zone topographies considered in section 8. Orange discs – RRP vesicles, green discs – Ca^{2+} channels, black spots – Ca^{2+} sensors of exocytosis, violet area – presynaptic density.

8.2 Active zones with 1 vesicular release site and N Ca^{2+} channels, one set of Ca^{2+} buffers

Let us next consider a situation equivalent to that introduced in the previous section, except that we now assume the presence of one presynaptic mobile Ca^{2+} buffer. As it was shown in section 7.4, the linearized approximation of Ca^{2+} dynamics works well for the synapse considered in this work⁹. Then, the time-averaged stationary spatial Ca^{2+} concentration profile resulting from a single Ca^{2+} channel in the presence of a Ca^{2+} buffer with a single binding site reads as (3):

$$\delta\langle[\text{Ca}^{2+}]\rangle_i = \frac{i_{Ca} \cdot P_o}{4 \cdot \pi \cdot F \cdot (\kappa \cdot D_B + D) \cdot R_i} \cdot \left(1 + \frac{\kappa \cdot D_B}{D} \cdot e^{-R_i/\lambda}\right) = \frac{i_{Ca} \cdot P_o}{R_i} \cdot (A + B \cdot e^{-R_i/\lambda}), \quad [3]$$

where D_B is diffusion coefficient of the buffer molecules, κ and λ are parameters dependent on the resting Ca^{2+} concentration, Ca^{2+} binding and unbinding rates of the buffer as well as D and D_B (see (3) for quantitative definition of κ and λ). Let us now, as in the previous section, assume that we estimate $\langle[\text{Ca}^{2+}]\rangle$ at the vesicular release site based on an experimentally measured amount of exocytosis: $\langle[\text{Ca}^{2+}]\rangle = f^{-1}(\Delta_{rel.})$. Then, we can apply the single Ca^{2+} source model and estimate the effective coupling distance R_c by solving the following equation:

$$\langle[\text{Ca}^{2+}]\rangle = \frac{I_{Ca} \cdot P_o}{R_c} \cdot (A + B \cdot e^{-R_c/\lambda}) \rightarrow R_c. \quad [4]$$

⁹This assumption is applied to all the situations considered in sections 8.2-8.5 whenever the presence of Ca^{2+} buffers is assumed.

If we denote $\delta\langle[\text{Ca}^{2+}]\rangle_i = g(R_i)$, equation [4] can be written in the following way:

$$R_c = g^{-1}\left(\frac{\langle[\text{Ca}^{2+}]\rangle}{N}\right) = g^{-1}\left(\frac{1}{N}\sum_{i=1}^N g(R_i)\right) \equiv \langle R \rangle_{Ca}^{\mathcal{N}}, \quad [5]$$

Thus, in this case, R_c can be interpreted as a nonlinear average, which we denote by $\langle R \rangle_{Ca}^{\mathcal{N}}$, of R_i s implicitly weighted by contributions of the corresponding channels to $\langle[\text{Ca}^{2+}]\rangle$. Here, superscript \mathcal{N} stands for “nonlinear”. The higher the contribution of a channel to $\langle[\text{Ca}^{2+}]\rangle$ and, thus, exocytosis, the closer $\langle R \rangle_{Ca}^{\mathcal{N}}$ is to the distance from that channel to the Ca^{2+} sensor of exocytosis. Equation [5] is valid for any arbitrary well defined dependence of $\delta\langle[\text{Ca}^{2+}]\rangle_i$ on R_i , for example, the one in the presence of multiple mobile Ca^{2+} buffers in the presynaptic solution.

It follows from equation [5] that $\langle R \rangle_{Ca}^{\mathcal{N}} = \langle R \rangle_{Ca}^{\mathcal{L}} = R_i$ if all the channels are equidistant to the Ca^{2+} sensor, i.e., $R_i = R_j$ for any i and j . If the channels are not equidistant, $\langle R \rangle_{Ca}^{\mathcal{N}} \neq \langle R \rangle_{Ca}^{\mathcal{L}}$. However, note that at sufficiently small distances, i.e., when $R_i \ll \lambda$, and at sufficiently large distances, i.e., when $R_i \gg \lambda$, $\delta\langle[\text{Ca}^{2+}]\rangle_i$ is approximately inversely proportional to R_i even in the presence of Ca^{2+} buffers. This statement follows from equation [3], see also (3). Thus, if a fraction of the channels is sufficiently close to the Ca^{2+} sensor, while the remaining channels are sufficiently far away from the Ca^{2+} sensor, $\langle R \rangle_{Ca}^{\mathcal{N}} \approx \langle R \rangle_{Ca}^{\mathcal{L}}$.

To estimate how big the difference between $\langle R \rangle_{Ca}^{\mathcal{N}}$ and $\langle R \rangle_{Ca}^{\mathcal{L}}$ might be in Ca^{2+} buffering conditions used in this work, we considered a Ca^{2+} channel cluster consisting of 2 to 5 channels, which were distributed in a 2D area, like in **Fig. S12A**. Each of the channels was located from the Ca^{2+} sensor of exocytosis not closer than 1 nm and not further than 100 nm. 0.5 mM and 1 mM of either BAPTA or EGTA were considered as presynaptic Ca^{2+} buffers. To estimate the maximum and the minimum values of the difference $\langle R \rangle_{Ca}^{\mathcal{N}} - \langle R \rangle_{Ca}^{\mathcal{L}}$, we used the optimization based on a genetic algorithm (MATLAB function *ga*, *Generations*=20 · *N*, *StallGenLimit*=15 · *N*, *PopulationSize*=*N* · 50, *EliteCount*=*N* · 5, *CrossoverFraction*=0.6, *TolFun*=10⁻¹²) followed by Nelder-Mead simplex method (MATLAB function *fminsearch*) repeated with 100 different initial conditions. In all these cases considered, the numerical optimization suggested that $\langle R \rangle_{Ca}^{\mathcal{N}} \geq \langle R \rangle_{Ca}^{\mathcal{L}}$ with the equality between the two present only when all the Ca^{2+} channels were equidistant to the sensor. $\max[\langle R \rangle_{Ca}^{\mathcal{N}} - \langle R \rangle_{Ca}^{\mathcal{L}}]$ was larger for buffers with smaller parameter λ , and for larger *N*, as summarized in **Table S1**.

| | $\max[\langle R \rangle_{Ca}^{\mathcal{N}} - \langle R \rangle_{Ca}^{\mathcal{L}}], \text{ nm}$ | | | |
|---------|---|-----------|--------------|------------|
| | 0.5 mM EGTA | 1 mM EGTA | 0.5 mM BAPTA | 1 mM BAPTA |
| $N = 2$ | 3 | 4 | 9 | 9 |
| $N = 3$ | 4 | 6 | 14 | 14 |
| $N = 4$ | 5 | 7 | 17 | 17 |
| $N = 5$ | 6 | 7 | 19 | 19 |

Table S1

8.3 Active zones with 1 vesicular release site and N Ca^{2+} channels, two sets of Ca^{2+} buffers

As it is formulated in Methods, the single Ca^{2+} source model was designed to estimate the effective coupling distance R_c from experimental data in such a way that knowledge of the absolute values of $\langle[\text{Ca}^{2+}]\rangle$ at the vesicular release sites is not required¹⁰. Indeed, if we measure amounts of released vesicles in two different Ca^{2+} buffering conditions, then the ratio of these two estimates, $\Delta_{rel.,1}/\Delta_{rel.,2} = f(\langle[\text{Ca}^{2+}]_1\rangle)/f(\langle[\text{Ca}^{2+}]_2\rangle) = (\langle[\text{Ca}^{2+}]_1\rangle/\langle[\text{Ca}^{2+}]_2\rangle)^m$ can be used to extract the R_c :

$$\frac{\Delta_{rel.,1}}{\Delta_{rel.,2}} = \left(\frac{A_1 + B_1 \cdot e^{-R_c/\lambda_1}}{A_2 + B_2 \cdot e^{-R_c/\lambda_2}} \right)^m \rightarrow R_c \quad [6]$$

Here, A's and B's depend only on the physical parameters of the buffer molecules, their concentrations, diffusion coefficient of Ca^{2+} and the resting $[\text{Ca}^{2+}]$ at the presynaptic site. m is the apparent cooperativity of exocytosis¹¹. If we denote $\delta\langle[\text{Ca}^{2+}]_1\rangle_i = g_1(R_i)$, $\delta\langle[\text{Ca}^{2+}]_2\rangle_i = g_2(R_i)$, and $g_1(x)/g_2(x) = g_{12}(x)$, equation [6] can be rewritten in the following way:

$$R_c = g^{-1} \left(\frac{\langle[\text{Ca}^{2+}]_1\rangle}{\langle[\text{Ca}^{2+}]_2\rangle} \right) = g_{12}^{-1} \left(\frac{\sum_{i=1}^N g_1(R_i)}{\sum_{i=1}^N g_2(R_i)} \right) \equiv \langle R \rangle_{Ca,12}^*, \quad [7]$$

Here, subscript 12 stands for the two buffering conditions "1" and "2" used to estimate $\langle R \rangle_{Ca,12}^*$. The superscript * is used to emphasize that the effective coupling distance is calculated by estimating exocytosis in two different presynaptic Ca^{2+} buffering conditions "1" and "2". Like $\langle R \rangle_{Ca}^N$, $\langle R \rangle_{Ca,12}^*$ can be interpreted as a nonlinear average, of R_i s implicitly weighted by the contributions of the corresponding channels to $\langle[\text{Ca}^{2+}]\rangle$. However, in general, $\langle R \rangle_{Ca,12}^* \neq \langle R \rangle_{Ca,1}^N$ and $\langle R \rangle_{Ca,12}^* \neq \langle R \rangle_{Ca,2}^N$, unless all the Ca^{2+} channels are equidistant to the Ca^{2+} sensor of exocytosis, in which case $\langle R \rangle_{Ca,12}^* = \langle R \rangle_{Ca,1}^N = \langle R \rangle_{Ca,2}^N = R_i$. Clearly, equation [7] is valid for any arbitrary well defined dependence of $\delta\langle[\text{Ca}^{2+}]\rangle_i$ on R_i , for example, the one in the presence of multiple mobile Ca^{2+} buffers in the presynaptic solution.

That we do not need to know the absolute values of $\langle[\text{Ca}^{2+}]\rangle$ at the Ca^{2+} sensor of exocytosis or Ca^{2+} currents that give rise to $\langle[\text{Ca}^{2+}]\rangle$ in order to determine R_c as defined by equation [7] is a very important advantage of the mentioned approach over that considered in section 8.2. Indeed, $\langle[\text{Ca}^{2+}]\rangle$ at Ca^{2+} sensors of exocytosis is not a measurable quantity with currently available experimental techniques. On the other hand, this approach has one disadvantage, which always has to be kept in mind when interpreting estimates of R_c based on the experimental data. The disadvantage is that it is necessary to measure the release in at least two different Ca^{2+} buffering conditions, only one of which can be the natural one. Thus, an estimate of R_c achieved by using this approach depends not only on the intrinsic properties of the system being studied, but also on how we choose to study the system. It follows from equation [3] that, when the buffering length constant λ is decreased (by increasing concentration of the buffer, for example), the contribution of a particular channel to $\langle[\text{Ca}^{2+}]\rangle$ at a Ca^{2+} sensor of exocytosis is decreased the more the further that channel is away from the sensor. Thus, if mobile Ca^{2+} buffers used for estimating R_c are much stronger than the endogenous buffers of the synapse, the coupling distance may be

¹⁰ Assuming the linearity between i_{Ca} and $\langle[\text{Ca}^{2+}]\rangle$ at the vesicular release sites.

¹¹ Here and further on, we assume that the apparent Ca^{2+} cooperativity is the same in both Ca^{2+} buffering conditions used for determining R_c .

considerably underestimated. Vice versa, if mobile Ca^{2+} buffers used for estimating R_c are much weaker than the endogenous buffers of the synapse, the coupling distance may be overestimated. Nevertheless, as it is shown next, $\langle R \rangle_{Ca,12}^{\mathcal{N}^*}$ is closely related to quantities uniquely determined by the configuration of the natural system, for example, $\langle R \rangle_{Ca,1}^{\mathcal{L}}$ or $\langle R \rangle_{Ca,2}^{\mathcal{L}}$, and carries valuable information about the system if the experiment is designed appropriately. Noteworthy, if spatially resolved simulations are performed to check the hypothesis of particular scenarios of the active zone organization, the experimental estimate of R_c can be directly compared to its modeled counterpart independently of the buffering conditions¹².

To better understand the physical meaning of $\langle R \rangle_{Ca,12}^{\mathcal{N}^*}$, we compared it with linear weighted average distances $\langle R \rangle_{Ca,1}^{\mathcal{L}}$ and $\langle R \rangle_{Ca,2}^{\mathcal{L}}$, estimated separately in the two Ca^{2+} buffering conditions used for estimating $\langle R \rangle_{Ca,12}^{\mathcal{N}^*}$ ¹³. To this end, we first considered the previously introduced active zone model consisting of one vesicular release site and two to five Ca^{2+} channels (see section 8.2). Pairs constructed from four Ca^{2+} buffers introduced above were considered, namely: 1 mM BAPTA & 0.5 mM BAPTA, 1 mM BAPTA & 1 mM EGTA, 1 mM BAPTA & 0.5 mM EGTA, 0.5 mM BAPTA & 1 mM EGTA, 1 mM EGTA & 0.5 mM EGTA and 0.5 mM BAPTA & 0.5 mM EGTA. Numerical global optimization (performed in the same way as introduced in section 8.2) resulted in $\langle R \rangle_{Ca,2}^{\mathcal{L}} > \langle R \rangle_{Ca,12}^{\mathcal{N}^*} > \langle R \rangle_{Ca,1}^{\mathcal{L}}$ for buffers “1” and “2” with $\lambda_2 > \lambda_1$.

Next, we got estimates of $\langle R \rangle_{Ca,1}^{\mathcal{L}}$, $\langle R \rangle_{Ca,2}^{\mathcal{L}}$, and $\langle R \rangle_{Ca,12}^{\mathcal{N}^*}$ for examples of physiologically realistic active zone topographies. To this end, we studied three IHC active zone topography scenarios – M1, M2, and M3 – considered in (2), see **Fig. S12B-D**. In those three scenarios, 14 readily releasable pool vesicles (orange disks, $R = 20$ nm) were randomly distributed at the longer sides of the presynaptic density (violet rectangle). All the Ca^{2+} sensors of exocytosis (black dots) were located at the level of the plasma membrane, at the longer sides of the presynaptic density. In scenario M1, 50 Ca^{2+} channels (green disks, $R = 7.5$ nm) were distributed randomly within the presynaptic density. In scenario M2, 36 out of 50 Ca^{2+} channels were distributed randomly within the presynaptic density, while the remaining 14 Ca^{2+} channels were placed in contact with the Ca^{2+} sensors of exocytosis. In scenario M3, there were only 14 Ca^{2+} channels in contact with the Ca^{2+} sensors. We considered 100 active zone realizations for each scenario. Four pairs of mobile Ca^{2+} buffer sets, the same as those used in our experiments, were assumed: 1 mM BAPTA + 2mM ATP & 0.5 mM BAPTA + 2mM ATP, 1 mM BAPTA + 2 mM ATP & 1 mM EGTA + 2 mM ATP, 1 mM BAPTA + 2mM ATP & 0.5 mM EGTA + 2 mM ATP, and 1 mM BAPTA + 2 mM ATP & 2 mM ATP. Mouth of each Ca^{2+} channel was treated as a hemispherical source with 1 nm radius and $i_{Ca} = 0.3$ pA. $\langle R \rangle_{Ca,1}^{\mathcal{L}}$, $\langle R \rangle_{Ca,2}^{\mathcal{L}}$, and $\langle R \rangle_{Ca,12}^{\mathcal{N}^*}$ were estimated for each active zone scenario as averages over separate vesicular release sites within a particular realization of the active zone and over 100 realizations of that active zone scenario. The results are summarized in **Table S2**.

We found that, as in the case of the simplified active zone model considered before, inequality $\langle R \rangle_{Ca,2}^{\mathcal{L}} > \langle R \rangle_{Ca,12}^{\mathcal{N}^*} > \langle R \rangle_{Ca,1}^{\mathcal{L}}$ holds for active zone scenarios M1, M2, and M3. $\langle R \rangle_{Ca,12}^{\mathcal{N}^*}$ was shifted more towards $\langle R \rangle_{Ca,1}^{\mathcal{L}}$ than to $\langle R \rangle_{Ca,2}^{\mathcal{L}}$. As expected, values of $\langle R \rangle_{Ca,1}^{\mathcal{L}}$, $\langle R \rangle_{Ca,2}^{\mathcal{L}}$, and $\langle R \rangle_{Ca,12}^{\mathcal{N}^*}$ were the

¹²Of course, in this case, the exact value of R_c depends on the properties of the Ca^{2+} buffers used. However, now we need to use only one set of Ca^{2+} buffers. This set of buffers may be chosen, at least in principle, to be that which is present in a real synapse.

¹³The main reason why we chose $\langle R \rangle_{Ca,1}^{\mathcal{L}}$ and $\langle R \rangle_{Ca,2}^{\mathcal{L}}$, not $\langle R \rangle_{Ca,1}^{\mathcal{N}}$ and $\langle R \rangle_{Ca,2}^{\mathcal{N}}$, to compare to $\langle R \rangle_{Ca,12}^{\mathcal{N}^*}$ is that $\langle R \rangle_{Ca}^{\mathcal{L}}$ have a clearer physical meaning than $\langle R \rangle_{Ca}^{\mathcal{N}}$ (compare equations [2] and [5]).

| | | | “1” 1 mM BAPTA “2” 0.5 mM BAPTA (+2 mM ATP) | “1” 1 mM BAPTA “2” 0.5 mM EGTA (+2 mM ATP) | “1” 1 mM BAPTA “2” 1 mM EGTA (+2 mM ATP) | “1” 1 mM BAPTA “2” - (+2 mM ATP) |
|----|---|------|---|--|--|--|
| M1 | $\langle R \rangle_{Ca,1}^{\mathcal{L}}$ | (nm) | 35 | 35 | 35 | 35 |
| | $\langle R \rangle_{Ca,12}^{\mathcal{N}^*}$ | | 36 | 44 | 43 | 45 |
| | $\langle R \rangle_{Ca,2}^{\mathcal{L}}$ | | 40 | 65 | 62 | 70 |
| M2 | $\langle R \rangle_{Ca,1}^{\mathcal{L}}$ | (nm) | 19 | 19 | 19 | 19 |
| | $\langle R \rangle_{Ca,12}^{\mathcal{N}^*}$ | | 20 | 28 | 27 | 29 |
| | $\langle R \rangle_{Ca,2}^{\mathcal{L}}$ | | 24 | 47 | 44 | 52 |
| M3 | $\langle R \rangle_{Ca,1}^{\mathcal{L}}$ | (nm) | 10 | 10 | 10 | 10 |
| | $\langle R \rangle_{Ca,12}^{\mathcal{N}^*}$ | | 11 | 15 | 15 | 16 |
| | $\langle R \rangle_{Ca,2}^{\mathcal{L}}$ | | 12 | 26 | 24 | 29 |

Table S2

smallest for scenario M3 (the most tight coupling), and the largest for scenario M1 (the least tight coupling) at any buffering conditions considered. The largest difference between $\langle R \rangle_{Ca,2}^{\mathcal{L}}$ and $\langle R \rangle_{Ca,1}^{\mathcal{L}}$, which reflects the sensitivity of R_c estimate to the Ca^{2+} buffering conditions, was found for scenario M1 and the smallest – for scenario M3. This is partially explained by the fact that a tighter coupling with fewer channels contributing Ca^{2+} to particular vesicular release sites results in a smaller variability of the distances between the channels and the vesicular release site about the average one. Another reason is that the considered mobile Ca^{2+} buffers have a relatively small effect on $\delta\langle[\text{Ca}^{2+}]\rangle_i$ when the coupling is so tight as in scenario M3, as mentioned in section 8.2. The estimates of $\langle R \rangle_{Ca,1}^{\mathcal{L}}$, $\langle R \rangle_{Ca,2}^{\mathcal{L}}$, and $\langle R \rangle_{Ca,12}^{\mathcal{N}^*}$ were smaller with stronger Ca^{2+} buffering conditions. For example, in the case of scenario M1, $\langle R \rangle_{Ca,12}^{\mathcal{N}^*}$ was equal to 36 nm for 1 mM BAPTA + 2 mM ATP & 0.5 mM BAPTA + 2 mM ATP, compared to 45 nm for 1 mM BAPTA + 2 mM ATP & 2 mM ATP. This trend is explained by the fact that the relative contributions of more distant Ca^{2+} channels are reduced when the strength of the Ca^{2+} buffers is increased.

In conclusion, the results discussed in this section suggest that, at least for the Ca^{2+} buffering conditions considered in this work, $\langle R \rangle_{Ca,12}^{\mathcal{N}^*}$ can be treated as an upper or lower bound for $\langle R \rangle_{Ca}^{\mathcal{L}}$ estimated in the natural Ca^{2+} buffering conditions. $\langle R \rangle_{Ca,12}^{\mathcal{N}^*}$ is the upper bound for $\langle R \rangle_{Ca}^{\mathcal{L}}$ when buffer “2” is weaker, i.e., with higher λ , than the natural Ca^{2+} buffer in the synapse while buffer “1” is not stronger than the endogenous buffer. $\langle R \rangle_{Ca,12}^{\mathcal{N}^*}$ is the lower bound for $\langle R \rangle_{Ca}^{\mathcal{L}}$ when buffer “2” is not stronger than the endogenous Ca^{2+} buffer in the synapse while buffer “1” is stronger, i.e., with lower λ , than the natural buffer.

8.4 Active zones with M vesicular release sites and N Ca^{2+} channels

Real presynaptic active zones contain considerably more than one vesicular release site. If the dependence of vesicle release rate on $[\text{Ca}^{2+}]$ is non-linear, the interpretation of the effective coupling distance R_c for an active zone with $M > 1$ site is more complicated compared to the situations with $M = 1$ considered

so far¹⁴. To see this, let us consider an active zone with $M > 1$ vesicular release sites driven by N Ca^{2+} channels. As before, we assume that the contribution to the time-averaged Ca^{2+} concentration at a particular vesicular release site j by a particular channel i is a bijective function of the distance between the channel and the corresponding Ca^{2+} sensor of exocytosis: $\delta\langle[\text{Ca}^{2+}]\rangle_{j,i} = g(R_{j,i})$. We also assume that, for each vesicular release site, the amount of vesicles released in particular time window T depends only on time-averaged Ca^{2+} concentration at that vesicular release site: $\Delta_{rel.,j} = f(\langle[\text{Ca}^{2+}]\rangle_j) = f(\sum_{i=1}^N \delta\langle[\text{Ca}^{2+}]\rangle_{j,i})$. Then, R_c estimated by recording the amount of release at the active zone, $\Delta_{rel.,\Sigma} = \sum_{j=1}^M \Delta_{rel.,j}$, in the presence of a particular set of Ca^{2+} buffers can be expressed in the following way:

$$R_c = g^{-1}\left(\frac{1}{N}f^{-1}\left(\frac{1}{M}\sum_{j=1}^M f\left(\sum_{i=1}^N g(R_{j,i})\right)\right)\right). \quad [8]$$

Equation [8] is a generalization of equation [5] for active zones with an arbitrary number of vesicular release sites. R_c defined by equation [8] can be interpreted as a nonlinear, implicitly weighted average of distances between a particular channel and a particular Ca^{2+} sensor of exocytosis over all possible channel-sensor pairs. Differently from the situation with a single vesicular release site, the nonlinear averaging of distances between one of the Ca^{2+} channels and one of the Ca^{2+} sensors of exocytosis now depends not only on how $\delta\langle[\text{Ca}^{2+}]\rangle_{j,i}$ depends on $R_{j,i}$ but also on how $\Delta_{rel.,j}$ depends on $\langle[\text{Ca}^{2+}]\rangle_j$. Qualitatively, the larger the relative contribution of a particular Ca^{2+} channel to $\langle[\text{Ca}^{2+}]\rangle_j$ at a particular vesicular release site is and the larger the relative contribution of that vesicular release site to the overall release at the active zone $\Delta_{rel.,\Sigma}$ is, the closer is R_c to the distance between that particular Ca^{2+} channel and Ca^{2+} sensor of exocytosis of that particular vesicular release site.

If all vesicular release sites are equivalent in the sense of how the Ca^{2+} channels are positioned in regards of them, i.e., if $R_{j,i} = R_{j',i} \equiv R_i$ for any j, j' , and i , the effective coupling distance for the whole active zone is equal to the effective coupling distance for one of the vesicular release sites. Indeed, if that condition is met, equation [8] reduces to equation [5]. Equation [8] reduces to $R_c = R_{i,j}$ when $R_{i,j} = R_{i',j'}$ for arbitrary i, i', j , and j' . i.e., when all the Ca^{2+} channels are at the same distance from all the Ca^{2+} sensors. In this case, R_c is equal to the physical distance between any of those Ca^{2+} channels and any of those Ca^{2+} sensors of exocytosis at the active zone. If $\Delta_{rel.,j}$ depends on $\langle[\text{Ca}^{2+}]\rangle_j$ linearly, i.e., if $f(x) = a \cdot x + b$, the effective coupling distance R_c is equal to the effective coupling distance of the “average vesicular release site” within the active zone:

$$R_c = g^{-1}\left(\frac{1}{M}\sum_{j=1}^M \left(\frac{1}{N}\sum_{i=1}^N g(R_{j,i})\right)\right). \quad [9]$$

When dependence of $\Delta_{rel.,j}$ on $\langle[\text{Ca}^{2+}]\rangle_j$ follows a power law, i.e., when $f(x) = k \cdot x^m$, and no Ca^{2+} buffers are present in the presynaptic solution, i.e., when $\delta\langle[\text{Ca}^{2+}]\rangle_{j,i}$ is described by [1], [8] has the

¹⁴This is true independently of how many vesicles are actually released during the observation window.

following form:

$$\begin{aligned}
R_c &= g^{-1} \left(\frac{1}{N} \left(\frac{1}{M} \sum_{j=1}^M \left(\sum_{i=1}^N g(R_{j,i}) \right)^m \right)^{1/m} \right) = \frac{M \cdot N \cdot i_{Ca} \cdot P_o / (4 \cdot \pi \cdot F \cdot D)}{M \cdot \left(\frac{1}{M} \sum_{j=1}^M \left(\sum_{i=1}^N g(R_{j,i}) \right)^m \right)^{1/m}} = \\
&= \frac{\sum_{j=1}^M \sum_{i=1}^N R_{j,i} \cdot g(R_{j,i})}{M \cdot \left(\frac{1}{M} \sum_{j=1}^M \left(\sum_{i=1}^N g(R_{j,i}) \right)^m \right)^{1/m}} = \\
&= \sum_{j=1}^M \sum_{i=1}^N R_{j,i} \cdot \left(\frac{\delta \langle [\text{Ca}^{2+}]_{j,i} \rangle}{M \cdot \left(\frac{1}{M} \sum_{j'=1}^M \left(\sum_{i'=1}^N \delta \langle [\text{Ca}^{2+}]_{j',i'} \rangle \right)^m \right)^{1/m}} \right) \equiv \langle \langle R \rangle \rangle_{Ca}^{\mathcal{L},m}. \tag{10}
\end{aligned}$$

Here, $\left(\frac{1}{M} \sum_{j'=1}^M \left(\sum_{i'=1}^N \delta \langle [\text{Ca}^{2+}]_{j',i'} \rangle \right)^m \right)^{1/m}$ is the power m mean (Hölder mean) of $\langle [\text{Ca}^{2+}] \rangle_{j'}$ over all M vesicular release sites at the active zone. Thus, the effective coupling distance R_c , in this case, is a weighted linear average of distances from all the Ca^{2+} channels to all the Ca^{2+} sensors in the active zone, which we denote by $\langle \langle R \rangle \rangle_{Ca}^{\mathcal{L},m}$. Here, the second angular brackets stand for averaging over vesicular release sites (in addition to the averaging over Ca^{2+} channels). The superscript m expresses the idea that the effective coupling distance depends on the apparent Ca^{2+} cooperativity of exocytosis. The weight for distance $R_{j,i}$ between channel i and vesicular release site j is equal to the ratio between the increment of Ca^{2+} concentration at the vesicular release site j contributed by the channel i and the power m mean of Ca^{2+} concentrations over all vesicular release sites at the active zone multiplied by the number of the vesicular release sites. It follows from the properties of the Hölder mean that $\left(\frac{1}{M} \sum_{j'=1}^M \left(\sum_{i'=1}^N \delta \langle [\text{Ca}^{2+}]_{j',i'} \rangle \right)^{m_2} \right)^{1/m_2} > \left(\frac{1}{M} \sum_{j'=1}^M \left(\sum_{i'=1}^N \delta \langle [\text{Ca}^{2+}]_{j',i'} \rangle \right)^{m_1} \right)^{1/m_1}$ for $m_2 > m_1$. Thus, the higher is Ca^{2+} cooperativity of exocytosis, the smaller is $\langle \langle R \rangle \rangle_{Ca}^{\mathcal{L},m}$.

When R_c is estimated by using the measurements of $\Delta_{rel,\Sigma}$ in two different Ca^{2+} buffering conditions¹⁵ and $f(x) = k \cdot x^m$, the equivalent of equation [8] reads as

$$R_c = g_{12}^{-1} \left(\left(\frac{\sum_{j=1}^M \left(\sum_{i=1}^N g_1(R_{j,i}) \right)^m}{\sum_{j=1}^M \left(\sum_{i=1}^N g_2(R_{j,i}) \right)^m} \right)^{1/m} \right) \equiv \langle \langle R \rangle \rangle_{Ca,12}^{\mathcal{N},m}, \tag{11}$$

where $g_1(R_{j,i})$ and $g_2(R_{j,i})$ are dependencies of $\langle [\text{Ca}^{2+}] \rangle_{j,i}$ on $R_{j,i}$ in Ca^{2+} buffering conditions “1” and “2” respectively, $g_{12}(x) = g_1(x)/g_2(x)$. Taking into account the results from section 8.3, it is tempting to hypothesize that $\langle \langle R \rangle \rangle_{Ca,12}^{\mathcal{N},m}$ could be an upper and a lower bound for $\langle \langle R \rangle \rangle_{Ca,1}^{\mathcal{L},m}$ and $\langle \langle R \rangle \rangle_{Ca,2}^{\mathcal{L},m}$, respectively, and could be rather well approximated by the average of the later two. We checked this idea with the realistic active zone topographies considered in section 8.3 and shown in **Fig. S12B-D**. The results of our simulations for $m = 1.7$, the experimentally predicted value of the apparent Ca^{2+} cooperativity of exocytosis (see **Fig. S6**), are summarized in **Table S3**. The results are strikingly similar to those for $\langle R \rangle_{Ca,1}^{\mathcal{L}}$, $\langle R \rangle_{Ca,12}^{\mathcal{N}}$, and $\langle R \rangle_{Ca,2}^{\mathcal{L}}$, shown in **Table S2**¹⁶. Thus, all the conclusions and comments made at the end of section 8.3 in the context of an active zone with a single vesicular release site, are valid for R_c estimated for scenarios M1, M2, and M3 with all vesicular release sites within an active zone considered collectively.

¹⁵As it was done in our study.

¹⁶We also considered higher m values. As mentioned before, R_c estimates are smaller for larger m . However, for active zone topographies scenarios M2 and M3, $m = 5$ resulted in estimates of $\langle \langle R \rangle \rangle_{Ca,12}^{\mathcal{N},m}$ only < 1 nm smaller than those for

| | | | “1” 1 mM BAPTA “2” 0.5 mM BAPTA (+2 mM ATP) | “1” 1 mM BAPTA “2” 0.5 mM EGTA (+2 mM ATP) | “1” 1 mM BAPTA “2” 1 mM EGTA (+2 mM ATP) | “1” 1 mM BAPTA “2” - (+2 mM ATP) |
|----|--|------|---|--|--|--|
| M1 | $\langle\langle R \rangle\rangle_{Ca,1}^{\mathcal{L},m}$ | (nm) | 31 | 31 | 31 | 31 |
| | $\langle\langle R \rangle\rangle_{Ca,12}^{\mathcal{N}*,m}$ | | 32 | 41 | 40 | 42 |
| | $\langle\langle R \rangle\rangle_{Ca,2}^{\mathcal{L},m}$ | | 37 | 63 | 60 | 68 |
| M2 | $\langle\langle R \rangle\rangle_{Ca,1}^{\mathcal{L},m}$ | (nm) | 19 | 19 | 19 | 19 |
| | $\langle\langle R \rangle\rangle_{Ca,12}^{\mathcal{N}*,m}$ | | 20 | 28 | 28 | 30 |
| | $\langle\langle R \rangle\rangle_{Ca,2}^{\mathcal{L},m}$ | | 24 | 47 | 44 | 51 |
| M3 | $\langle\langle R \rangle\rangle_{Ca,1}^{\mathcal{L},m}$ | (nm) | 10 | 10 | 10 | 10 |
| | $\langle\langle R \rangle\rangle_{Ca,12}^{\mathcal{N}*,m}$ | | 11 | 15 | 15 | 16 |
| | $\langle\langle R \rangle\rangle_{Ca,2}^{\mathcal{L},m}$ | | 12 | 26 | 24 | 29 |

Table S3

Finally, we have to note that we used estimates of capacitance increments in four different pairs of Ca^{2+} buffering conditions collectively to estimate the R_c (see Methods). This was done with the purpose to reduce the influence of measurement noise in the experimental data. Thus, in order to interpret the experimental estimate of R_c in the context of spatially resolved active zone models, we have to estimate the same quantity for those modeled active zones. The corresponding model estimates of R_c calculated in the mentioned way were 41 nm, 28 nm, and 15 nm for scenarios M1, M2, and M3, respectively. Thus, our experimental estimate $R_c = 17$ nm with 5 – 95 percentile range of 8 – 30 nm (see Results) for the single Ca^{2+} source model is compatible with the active zone topography scenarios M2 and M3 but not scenario M1.

8.5 Influence of the Ca^{2+} channel opening-closing dynamics on R_c estimate

All considerations related to R_c in sections 8.1-8.4 were based on the assumption that exocytosis rate at any vesicular release site is a well defined function of the time-averaged stationary Ca^{2+} concentration at that vesicular release site. In our experiments, cumulative release was measured 20 ms after the stimulus onset. 20 ms is much longer than the characteristic equilibration time of the channel opening, which is 0.5 ms at the membrane potential corresponding to the peak Ca^{2+} current in IHCs (18). Thus, the assumption of stationarity is justified. However, “averaging out” the fluctuations of Ca^{2+} concentration due to opening and closing of the presynaptic Ca^{2+} channels may still substantially influence the results, if channel gating is not sufficiently fast¹⁷. To check this averaging assumption we performed additional simulations where the build-up and decay of $[\text{Ca}^{2+}]$ due to the channel gating was modeled explicitly as it was done in (2). We assumed a three state Markov model of the channel gating: $C_1 \xrightleftharpoons[1 \cdot k_{-1}]{2 \cdot k_{+1}} C_2 \xrightleftharpoons[2 \cdot k_{-1}]{1 \cdot k_{+1}} O$, $k_1 = 1.78 \text{ ms}^{-1}$, $k_{-1} = 1.37 \text{ ms}^{-1}$. Vesicle fusion followed the kinetic model proposed by (19). All the

$m = 1.7$. For scenario M1, the differences were not larger than 4 nm, which is still small compared to the absolute values of $\langle\langle R \rangle\rangle_{Ca,12}^{\mathcal{N}*,m}$. Thus, at least for the considered active zone topographies, m does not affect value of R_c considerably.

¹⁷By speed of channel gating we mean the closing and opening rates of the channel.

kinetic parameters of vesicle fusion were set to the original values except that k_{on} was reduced four times in order to reproduce reasonable m and ΔC_m values. Vesicle replenishment was treated as a single step process with a fixed rate $k_{rep} = 0.13\text{ms}^{-1}$. Other relevant details of the simulation procedure are reported in (2).

Using the aforementioned model to calculate $\Delta_{rel.,\Sigma}$ and its dependence on $\langle[\text{Ca}^{2+}]\rangle$, we estimated the coupling distance R_c in the same way which was discussed in the last paragraph of section 8.4. The corresponding values of R_c for scenarios M1, M2, and M3 were 37 nm, 27 nm, and 14 nm, respectively. This is in a very good agreement with the estimates of R_c that were achieved by ignoring the fluctuations of $[\text{Ca}^{2+}]$ due to the $[\text{Ca}^{2+}]$ channels closing and opening. This result lets us conclude that, for active zone topographies and the kinetic parameters considered in this work, the channel gating noise does not considerably affect the estimation of R_c .

References

1. P. Heil, H. Neubauer, D.R.F. Irvine, and M. Brown. **Spontaneous activity of auditory-nerve fibers: insights into stochastic processes at ribbon synapses.** *J. Neurosci.* 2007, **27**: 8457 – 8474.
2. A.B. Wong, M.A. Rutherford, M. Gabrielaitis, T. Pangršič, F. Göttfert, T. Frank, S. Michanski, S. Hell, F. Wolf, C. Wichmann, and T. Moser. **Developmental refinement of hair cell synapses tightens the coupling of Ca^{2+} influx to exocytosis.** *EMBO J.* 2014, **33**: 247 – 264.
3. M. Naraghi and E. Neher. **Linearized buffered Ca^{2+} diffusion in microdomains and its implications for calculation of $[\text{Ca}^{2+}]$ at the mouth of a calcium channel.** *J. Neurosci.* 1997, **17**: 6961 – 6973.
4. U.V. Nägerl, D. Novo, I. Mody, and J.L. Vergara. **Binding kinetics of calbindin-D28k determined by flash photolysis of caged Ca^{2+} .** *Biophys. J.* 2000, **79**: 3009 – 3018.
5. J.H. Bollmann and B. Sakmann. **Control of synaptic strength and timing by the release-site Ca^{2+} signal.** *Nat. Neurosci.* 2005, **8**: 426 – 434.
6. S.H. Lee, B. Schwaller, and E. Neher. **Kinetics of Ca^{2+} binding to parvalbumin in bovine chromaffin cells: implications for $[\text{Ca}^{2+}]$ transients of neuronal dendrites.** *J Physiol.* 2000, **525**: 419 – 432.
7. G.C. Faas, S. Raghavachari, J.E. Lisman, and I. Mody. **Calmodulin as a direct detector of Ca^{2+} signals.** *Nat. Neurosci.* 2011, **14**: 301 – 304.
8. G.C. Faas, B. Schwaller, J.L. Vergara, and I. Mody. **Resolving the fast kinetics of cooperative binding: Ca^{2+} buffering by calretinin.** *Plos Biol.* 2007, **5**: e311.
9. H. Schmidt, E.B. Brown, B. Schwaller, and J. Eilers. **Diffusional mobility of parvalbumin in spiny dendrites of cerebellar Purkinje neurons quantified by fluorescence recovery after photobleaching.** *Biophys. J.* 2003, **84**: 2599 – 2608.
10. H. Schmidt, B. Schwaller, and J. Eilers. **Calbindin D28k targets myo-inositol monophosphatase in spines and dendrites of cerebellar Purkinje neurons** *PNAS* 2005, **102**: 5850 – 5855.
11. D. Beutner, T. Moser. **The presynaptic function of mouse cochlear inner hair cells during development of hearing.** *J. Neurosci.* 2001, **21**: 4593 – 4599.
12. A.C. Meyer, T. Frank, D. Khimich, G. Hoch, D. Riedel, N.M. Chapochnikov, Y.M. Yarin, B. Harke, S.W. Hell, A. Egner, and T. Moser. **Tuning of synapse number, structure and function in the cochlea.** *Nat. Neurosci.* 2009, **12**: 444 – 453.
13. D. Lenzi, J.W. Runyeon, J. Crum, M.H. Ellisman, and W.M. Roberts. **Synaptic vesicle populations in saccular hair cells reconstructed by electron tomography.** *J. Neurosci.* 1999, **19**: 119 – 132.
14. E. Neher. **Usefulness and limitations of linear approximations to the understanding of Ca^{2+} signals.** *Cell Calcium* 1998, **24**: 345 – 357.
15. J.D. Goutman and E. Glowatzki. **Time course and calcium dependence of transmitter release at a single ribbon synapse.** *PNAS* 2007, **104**: 16341 – 16346.
16. I. Bucurenciu, A. Kulik, B. Schwaller, M. Frotscher, and P. Jonas. **Nanodomain coupling between Ca^{2+} channels and Ca^{2+} sensors promotes fast and efficient transmitter release at a cortical GABAergic synapse.** *Neuron* 2008, **57**: 536 – 545.
17. N.P. Vyleta and P. Jonas. **Loose coupling between Ca^{2+} channels and release sensors at a plastic hippocampal synapse.** *Science* 2014, **343**: 665 – 670.
18. J. Neef, A. Gehrt, A.V. Bulankina, A.C. Meyer, D. Riedel, R.G. Gregg, N. Strenzke, and T. Moser. **The Ca^{2+} channel subunit $\beta 2$ regulates Ca^{2+} channel abundance and function in inner hair cells and is required for hearing.** *J. Neurosci.* 2009, **29**: 10730 – 10740.
19. D. Beutner, T. Voets, E. Neher, and T. Moser. **Calcium dependence of exocytosis and endocytosis at the cochlear inner hair cell afferent synapse.** *Neuron* 2001, **29**: 681 – 690.